NEUROIMMUNOLOGY

# Immaturity of immune cells around the dural venous sinuses contributes to viral meningoencephalitis in neonates

**Young-Chan Kim[1,2,3]†, Ji Hoon Ahn[2]†‡*, Hokyung Jin[1,2], Myung Jin Yang[1,2], Seon Pyo Hong[2], Jin-Hui Yoon[2], Sang-Hoon Kim[1], Tirhas Niguse Gebre[1], Hyuek Jong Lee[2], You-Me Kim[1], Gou Young Koh[1,2]‡***



**High neonatal susceptibility to meningitis has been attributed to the anatomical barriers that act to protect the central nervous system (CNS) from infection being immature and not fully developed. However, the mechanisms by which pathogens breach CNS barriers are poorly understood. Using the Armstrong strain of lymphocytic choriomeningitis virus (LCMV) to study virus propagation into the CNS during systemic infection, we demonstrate that mortality in neonatal, but not adult, mice is high after infection. Virus propagated extensively from the perivenous sinus region of the dura mater to the leptomeninges, choroid plexus, and cerebral cortex. Although the structural barrier of CNS border tissues is comparable between neonates and adults, immunofluorescence staining and single-cell RNA sequencing analyses revealed that the neonatal dural immune cells are immature and predominantly composed of CD206$^{hi}$ macrophages, with major histocompatibility complex class II (MHCII)$^{hi}$ macrophages being rare. In adults, however, perivenous sinus immune cells were enriched in MHCII$^{hi}$ macrophages that are specialized for producing antiviral molecules and chemokines compared with CD206$^{hi}$ macrophages and protected the CNS against systemic virus invasion. Our findings clarify how systemic pathogens enter the CNS through its border tissues and how the immune barrier at the perivenous sinus region of the dura blocks pathogen access to the CNS.**

## INTRODUCTION

Neuroinfectious diseases are among the most devastating illnesses and can cause severe morbidity and mortality (*1*). To maintain an immune-privileged central nervous system (CNS) environment, multiple anatomical barriers including the blood-brain barrier (BBB) and blood–cerebrospinal fluid (CSF) barrier (BCSFB) protect the CNS (*2*). Despite the multiple barriers covering the CNS, systemic pathogens sometimes invade the CNS and propagate, leading to uncontrolled immune cell trafficking into the CNS (*3*–*6*). Exploring the underlying mechanisms of how and where systemic pathogens breach CNS barriers is thus important.

A minimum threshold of pathogen in the bloodstream is required to cause meningeal invasion (*5*); however, the route taken by pathogens penetrating the CNS has not been precisely elucidated. Previous research has focused on the perivascular spaces of the leptomeninges and choroid plexus (CP) as primary sites of systemic virus entry into the CNS (*1*), but the outcomes were based on disease-progressed human samples or models involving pathogen injection into the brain, which do not reflect the natural infection route. Furthermore, despite the substantial disease burden with long-term neurologic sequelae in neonatal meningitis (*7*), it is still unclear why neonates are more susceptible to CNS infection with pathogens that are normally blocked from reaching the CNS in adults. Several presumable causes, including direct exposure to the pathogen-rich birth canal, CNS barriers being immature in neonates, and unestablished cellular and humoral immunity, have been suggested (*6*, *8*, *9*), but key contributors to the high susceptibility are poorly understood.

The CNS borders—meninges, CP, and skull bone marrow—constitute a functional barrier at CNS interfaces, with resident immune cells that vigilantly patrol the CNS borders (*10*). Recent research has led to a deeper and more extensive understanding of CNS immunosurveillance (*11*, *12*). Each CNS border tissue is compartmentalized and shaped as a distinct immunologic niche for CNS immunosurveillance under normal conditions (*13*). Among these border tissues, the CP and leptomeninges are classically known to serve as gateways for immune cells and pathogens (*14*). In comparison, the dura mater (dura) has been considered a peripheral tissue physically separated from the CNS by the tight arachnoid barrier (*15*). However, emerging evidence highlights the dura as a key strategic site of immune surveillance for the CNS (*11*, *16*–*18*). The immune cells along the venous sinuses at the dura serve as a hub for relaying CNS-derived antigens (*18*). Moreover, CNS antigen–specific adaptive immune cells at the dura play critical roles in aggravating CNS autoimmune diseases (*16*–*18*).

Nevertheless, there is some controversy about the roles of the dural immune system in the pathogenesis of CNS autoimmune diseases: Not only is CNS antigen–specific T cell trafficking confined to the leptomeninges but CNS antigens are also not very accessible to the dura (*19*). Considering the peripheral location of the dura, clarifying the specific responses of the dural immune system to systemic pathogens is important and beginning to be understood (*20*). Although adaptive immune cells such as plasma cells at the dural

[1]Graduate School of Medical Science and Engineering, Korea Advanced Institute of Science and Technology, Daejeon 34141, Republic of Korea. [2]Center for Vascular Research, Institute for Basic Science (IBS), Daejeon 34141, Republic of Korea. [3]Department of Internal Medicine, Seoul National University Hospital, Seoul 03080, Republic of Korea.
*Corresponding author. Email: ahnadun@kaist.ac.kr (J.H.A.); gykoh@kaist.ac.kr (G.Y.K.)
†These authors equally contributed to this work.
‡These authors contributed equally to this work.

venous sinus protect against fungal infection (*21*), an understanding of how innate immune cells respond to peripheral pathogens has been elusive. Border-associated macrophages—innate immune cells that function in host defense and maintain tissue homeostasis—include major histocompatibility complex class II (MHCII)$^{hi}$ and MHCII$^{lo}$ macrophages and are extensively distributed in CNS border tissues (*20*, *22*, *23*). A recent report (*24*) demonstrates that the border-associated macrophages serve as the immune barrier for CNS protection but subsequently facilitate monocyte infiltration across the CNS border tissues when the *Trypanosoma brucei* parasite invades the border tissues. However, how the border-associated macrophages shape and establish cellular and functional innate immune barriers in these tissues is poorly understood.

Here, we show that MHCII$^{hi}$ macrophages at the perivenous sinus within the dura play a crucial role in preventing virus propagation into the CNS during early systemic infection. They are dynamically recruited to the perivenous sinus from the systemic circulation in an adhesion molecule–dependent manner during the postnatal period. The immaturity of this immune barrier at the perivenous sinus allows pathogen entry from the systemic circulation into the CNS in neonatal mice.

## RESULTS

### The dural venous sinus is an initial entry site for systemically invading LCMV

Given that neonates show a high susceptibility to meningitis caused by hematogenous pathogens (*5*), we hypothesized that the CNS barriers of neonatal mice would be immature and defective, allowing systemic entry of microbes into the CNS. To test this hypothesis, we intraperitoneally injected Armstrong strain lymphocytic choriomeningitis virus (LCMV), a noncytolytic rodent virus that infects CNS border tissues, including meninges, CP, and the ependymal cell layer (*25*, *26*), into postnatal day 7 (P7, neonates) or 4-week-old (P28, young adult) mice (Fig. 1A). The neonates died within 2 weeks after systemic LCMV infection, whereas young adult mice did not show any lethality (Fig. 1B). In line with this finding, LCMV particles were detected primarily in the perivenous sinus region of the dura (called the "perisinus" hereafter) at days postinfection (dpi) 4 and 6 in neonates (Fig. 1, C, D, and G), infecting particularly vimentin-positive stromal cells (fig. S1, A to C). At dpi 6, LCMVs were detected in perivascular space from the medial side (adjacent to the venous sinus) of the leptomeninges and cerebral cortex (we designate these regions together as the "LM-CC") but not in the CP in the neonates (Fig. 1C and fig. S1, G and H). To exclude the possibility that LCMV reached the LM-CC by leakage from brain vessels, we systemically injected fluorescence-labeled ovalbumin (Fluor-OVA) into neonates at dpi 6 after the systemic LCMV infection (fig. S1, E to H). No Fluor-OVA was detected in LCMV-infected LM-CC, whereas widespread Fluor-OVA was detected in the dura and CP (fig. S1, F to H). These findings indicate that LCMV propagates from the dura to the LM-CC rather than directly from the systemic circulation to the LM-CC in neonates.

At dpi 8, LCMV propagation was extensively found in all three regions including the epithelial cells of the CP and brain parenchymata in the neonates (Fig. 1, C, E, H, and I, and fig. S1D). In comparison, no LCMV propagation was detected in the CNS border tissues or brain parenchyma at any time point, except for the transient appearance of LCMV in the dura at dpi 4 in young adult mice (Fig. 1C). In line with these histological findings, reverse transcription polymerase chain reaction (RT-PCR) analysis revealed that LCMV viral transcripts were increased exponentially in the dura and to a lesser extent in the LM-CC and CP up to dpi 8 in neonates (Fig. 1F). In parallel, we observed that massive infiltration by CCR2$^{+}$MHCII$^{-}$Iba1$^{-}$ myelomonocytic cells was accompanied by LCMV propagation in the perisinus and LM-CC, but not the CP, in neonates (fig. S2, A to C), indicating that the CP is not the main route for inflammatory cell recruitment into the CNS upon viral infection. These data suggested that the dura has a barrier system specialized in preventing pathogen entry from the systemic circulation in young adult mice. To investigate this, we directly injected $3 \times 10^5$ plaque-forming units of LCMV into the cranial cavity via the cisterna magna [intracisterna magna (i.c.m.)] in adult mice (fig. S2D). In contrast to the findings of systemic LCMV (Fig. 1), we detected high levels of LCMV in the perisinus, LM-CC, and CP at dpi 3 and dpi 6, resulting in T cell recruitment into the perisinus and LM-CC and death within 8 days, consistent with a previous report (fig. S2, E to G) (*27*). Together, these findings signify that the dural venous sinus is the initial CNS entry site for systemic LCMV and imply that the perisinus serves as a barrier against LCMV invasion.

### The perisinus is devoid of a definitive tight barrier against systemic or CSF pathogen access in both neonates and adults

To delineate how the barrier system of the perisinus at the dura contributes to CNS protection against neurotropic pathogens, we compared the barrier features of each CNS border tissue between neonates and adult mice. In adults, vascular endothelial cells (ECs) of the dura and CP were equipped with high levels of plasmalemma vesicle–associated protein, whereas those of the LM-CC had high levels of claudin-5, a tight-junction molecule (fig. S3, A to C). Consistent with this finding, intravenously injected Fluor-OVA through the retro-orbital sinus was detected in perivascular macrophages of the dura and CP but not in the LM-CC (fig. S3, D to G). Fluor-OVA injected i.c.m. was detected in perivascular macrophages of the dura and LM-CC but not of the CP (fig. S3, H to K) and reached the perisinus beyond the subarachnoid space (fig. S3L), consistent with a previous report (*18*). Furthermore, intracerebroventricular-injected Fluor-OVA was detected in the large, Iba1$^{+}$ macrophages (fig. S3, M to O), which are likely "epiplexus macrophages" that are present along the apical epithelial surface (*28*), in the CP. These findings indicate the lack of a vascular barrier in the dura and the presence of a tight vascular barrier in the LM-CC and BCSFB in CP. This result highlights the perisinus' lack of any tight barrier against pathogen access from systemically circulating blood or CSF. Compared to young adult mice, neonates showed no notable differences in levels or distribution of claudin-5 and zonula occludens-1 (ZO-1) in vascular ECs of LM-CC and CP or CP epithelium (fig. S3P). Moreover, no differences were found in the distribution of systemically delivered Fluor-OVA at CNS borders between the two groups (fig. S3Q). Thus, neonates and adults have comparable tight barriers in the LM-CC and CP but lack a barrier in the perisinus against systemic or CSF pathogen access.

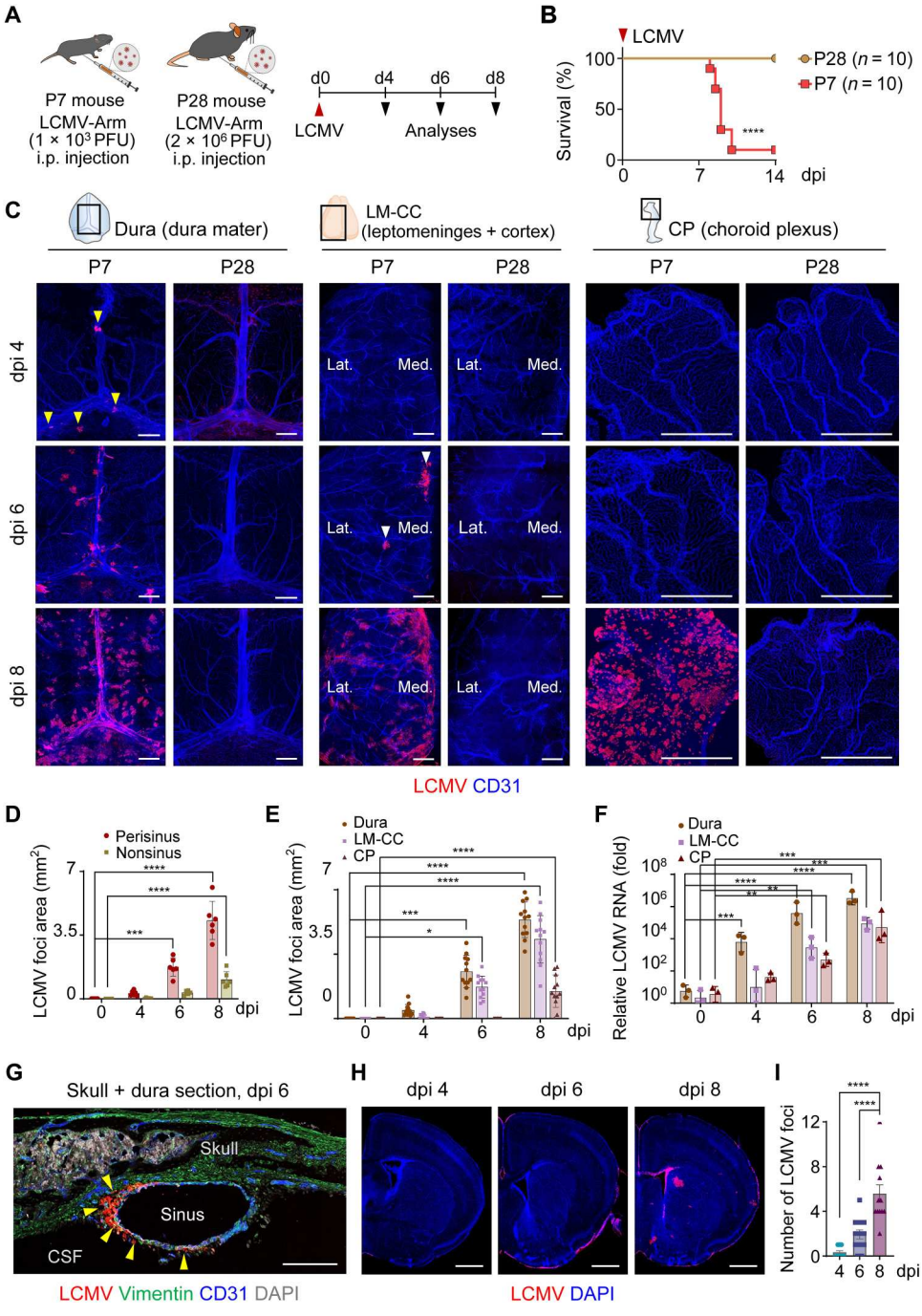


**Fig. 1. LCMV penetrates the perivenous sinus region of the dura mater and invades the CNS in neonatal mice.** (**A**) Diagram depicting the experimental procedure for intraperitoneal (i.p.) injection of the weight-adjusted amount of LCMV-Arm into P7 and P28 B6 mice and analyses at indicated dpi. (**B**) Survival rate of the indicated mice (each $n = 10$) after the LCMV-Arm infection. *P* values were calculated by log-rank test. (**C**) Representative immunofluorescence images of LCMV foci (red) and blood vessels (CD31, blue) at the dura (dura mater), LM-CC, and CP in P7 and P28 mice. Lat., lateral side; Med., medial side. Scale bars, 1.0 mm (dura, LM-CC) and 500 μm (CP). LCMV at the perivenous sinus region of the dura (perisinus) at 4 dpi (yellow arrowheads) and at the medial side of the LM-CC at 6 dpi (white arrowheads) in P7 mice. (**D** and **E**) Quantification of LCMV nucleoprotein (NP)–positive area at the perisinus and nonsinus regions of the dura, LM-CC, and CP from the neonates in (C). Each symbol represents data from an individual mouse; bars indicate mean ± SD. Data are derived from $n = 6$ to 12 mice per group pooled from three independent experiments. (**F**) Relative fold changes of LCMV glycoprotein RNA expression in the dura, LM-CC, and CP at indicated dpi of P7 mice after intraperitoneal administration of LCMV. Relative fold change was calculated by comparing threshold cycles ($2^{-\Delta\Delta Ct}$) of RT-PCR among three tissues. Each dot indicates a mean value from four mice, and bars indicate mean ± SD. $n = 12$ mice per group from three independent experiments. (**G**) Representative image from P7 mice showing LCMV (red) invasion into the perisinus (CD31, blue) at dpi 6, colocalized with vimentin-positive (green) stromal cells. Scale bar, 500 μm. Two independent experiments in $n = 4$ mice show similar findings. (**H** and **I**) Representative immunofluorescence images and the number of LCMV foci (red) in the brain parenchymata of the neonates. DAPI (blue) was used to outline brain tissue. Scale bars, 1.0 mm. Each symbol represents data from an individual mouse; bars indicate mean ± SD. Data are derived from $n = 12$ mice per group pooled from two independent experiments. *P* values in (D) to (F) and (I) were calculated using one-way ANOVA followed by Tukey's post hoc test. In all graphs, $^*P < 0.05$, $^{**}P < 0.01$, $^{***}P < 0.001$, and $^{****}P < 0.0001$. PFU, plaque-forming units.

## Abundant macrophages per se in the dura fail to limit virus dissemination in neonates

The above findings led us to compare resident immune barriers and their responses to viral invasion at the dura between neonates and young adult mice. To examine differences in resident immune cells at the dura, we intravenously injected fluorophore-labeled CD45 antibody (CD45iv) before perfusion and gated on $CD45iv^{-}CD45^{+}$ cells to exclude contamination by intravascular $CD45^{+}$ cells, in keeping with a previous report (*29*), before conducting single-cell RNA sequencing (scRNA-seq) (Fig. 2A). Unexpectedly, our scRNA-seq analysis of the dural extravascular $CD45^{+}$ cells revealed marked differences in types and fractions of immune cell subpopulations between the two groups (Fig. 2B). In neonates, most of the immune cells were macrophages, whereas in young adults, diverse and mature types of immune cell subpopulations were detected (Fig. 2, B and C, and fig. S4, A to C).

To identify critical cell types controlling the viral invasion of CNS border tissues, we pretreated recombination activating gene 2 (RAG2)–deficient mice with anti-CD90.2 antibody to deplete lymphoid lineage cells; wild-type (WT) mice with anti–Gr-1 antibody to deplete neutrophils and $Ly6C^{hi}$ monocytes; WT mice with a combination of anti–c-Kit antibody, anti–plasmacytoid

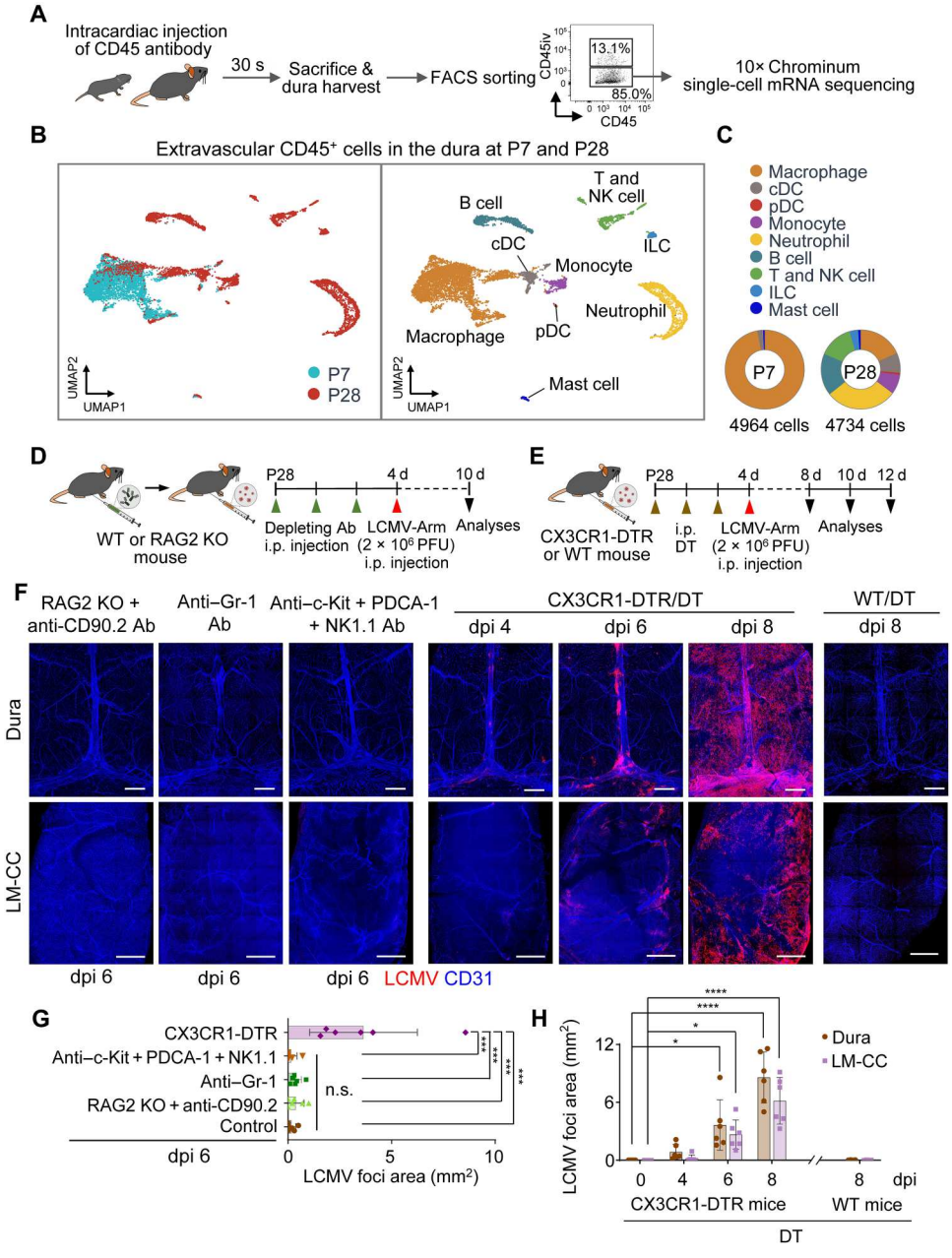


**Fig. 2. Abundant macrophages in the dura fail to limit viral dissemination in neonates.** (**A**) Experimental procedures of scRNA-seq for extravascular CD45$^+$ cells in the dura. CD45iv was intracardially given, followed by perfusion with ice-cold PBS for 30 s performed on normal P7 neonatal ($n$ = 30) and P28 young adult B6 mice ($n$ = 30). Leukocytes from the dura were gated for CD45iv$^-$CD45$^+$ cells to exclude contamination of intravascular CD45$^+$ cells and sorted for 10× chromium scRNA-seq. (**B**) UMAP plots visualizing extravascular CD45$^+$ cells in the dura of P7 (4964 cells) and P28 mice (4734 cells). (**C**) Donut plots show a fraction of each indicated cell cluster in the indicated total number of cells. ILC, innate lymphoid cell. (**D**) Diagram depicting the experimental procedure for intraperitoneal injections of cocktails of depleting antibodies (Abs) into P28 young WT B6 or RAG2-deficient mice, and then the mice are infected with intraperitoneal injection of LCMV-Arm and analyzed 6 days later. (**E**) Diagram depicting the experimental procedure for intraperitoneal injections of diphtheria toxin (DT) into P28 CX3CR1-DTR or WT B6 mice, and then the mice are infected with intraperitoneal injection of LCMV-Arm and analyzed indicated days later. (**F** to **H**) Representative immunofluorescence images and quantifications of LCMV foci (red) at the dura and LM-CC. CD31 (blue) for blood vessels showing the infection routes in the dura and LM-CC. Scale bars, 1.0 mm. Note that LCMV propagation is detected in the dura and LM-CC of CX3CR1-DTR mice but not in those of WT mice at dpi 8. In (G) and (H), bars indicate mean ± SD. Data are derived from $n$ = 4 to 6 mice per group pooled from two independent experiments. $P$ values in (G) and (H) were calculated using one-way ANOVA followed by Tukey's post hoc test. *$P$ < 0.05, ***$P$ < 0.001, and ****$P$ < 0.0001. n.s., not significant.

dendritic cell antigen-1 (PDCA-1) antibody, and anti-CD161 (NK1.1) antibody to deplete innate immune cells including mast cells, plasmacytoid dendritic cells, and NK cells; and CX3C chemokine receptor 1 (CX3CR1)–diphtheria toxin receptor (DTR) mice with diphtheria toxin to deplete macrophages (Fig. 2, D and E). We confirmed substantial depletion of targeted immune cells in the dura by flow cytometry analysis (fig. S5, A to D) and immunofluorescence staining (IFS) analysis (fig. S6, A and B). Nevertheless, among the groups, the macrophage-depleted CX3CR1-DTR mice showed apparent LCMV spread from the perisinus to the whole dura and LM-CC (Fig. 2, F to H, and fig. S6, C to G). Although intraperitoneal administrations of diphtheria toxin depleted most of the tissue-resident macrophages in the CNS borders and microglial cells in the brain parenchymata of the CX3CR1-DTR mice (fig. S6, A and B), no apparent LCMV foci were observed in the CP and brain parenchyma, whereas it was highly accumulated in the LM-CC at dpi 8 (fig. S6, C to G). As a control, diphtheria toxin–treated WT mice did not show the LCMV spread from the perisinus to the whole dura and LM-CC (Fig. 2, E, F, and H). These findings suggested that macrophages in the dura and LM-CC could serve as the initial defensive barrier against systemic pathogen invasion to the CNS before activation of the adaptive immune system. Nevertheless, our findings show that the abundant macrophages in the dura failed to limit virus dissemination in neonates (Figs. 1C and 2B). This raises the question of whether the difference in macrophage composition between neonates and young adult mice is a critical determinant of the high susceptibility of the neonates to LCMV-induced meningoencephalitis.

## MHCII$^{hi}$ cells at the perisinus are a distinct macrophage subpopulation in adult mice

To explore the differences and heterogeneity in dural macrophages between neonates and young adult mice, we subclustered the macrophage populations and compared them (Fig. 3A). Notably, most macrophages in neonates were CD206$^{hi}$ or proliferating macrophages, whereas a distinct MHCII$^{hi}$ macrophage population constituted a major type of the macrophages in young adult mice (Fig. 3, B and C). Intriguingly, compared with the CD206$^{hi}$ macrophages, MHCII$^{hi}$ macrophages highly expressed the transcripts of *Ccr2* (chemokine receptor), *Cxcl2*, *Ccl6*, *Ccl4* (chemokine), and *Il1b* (proinflammatory cytokine) (Fig. 3, D and F). Gene ontology analysis revealed that these MHCII$^{hi}$ macrophages were specialized for producing chemokines and mediating the inflammatory response (Fig. 3E). Consistent with these single-cell transcriptomic findings, two distinct macrophage subpopulations, MHCII$^{hi}$ and CD206$^{hi}$ macrophages, were identified by flow cytometric analysis in the dura of young adult mice (Fig. 3G). MHCII$^{hi}$ macrophages were CD206 negative or CD206 low, which is compatible with previous findings (Fig. 3G) (*22*, *30*). The spatial distribution patterns of these cells in the CNS borders of adult mice were distinct, with dense infiltration of MHCII$^{hi}$ cells in the perisinus and evenly dispersed CD206$^{hi}$ cells along the vascular network throughout the CNS borders (Fig. 3, H and I). We found that most of the MHCII$^{hi}$ cells in the perisinus were Iba1$^{+}$ macrophages, and they were distinct from the CD206$^{hi}$ macrophages, given that the most MHCII$^{hi}$ Iba1$^{+}$ macrophages were CD206 negative or CD206 low but CCR2 positive (Fig. 3J).

## MHCII$^{hi}$ cells are recruited along the venous sinus at the dura during the postnatal period

To investigate the emergence of MHCII$^{hi}$ cells in the dura, we used double Cx3cr1$^{+/GFP}$/Ccr2$^{+/RFP}$ neonatal mice and performed IFS for MHCII in CNS border tissues during the postnatal period. CX3CR1 single-positive cells, mainly CD206$^{hi}$ cells, were extensively distributed in CNS border tissues without notable changes throughout the postnatal period (Fig. 4, A and B, and fig. S7A). In contrast, the numbers of both CCR2$^{+}$ cells and MHCII$^{+}$ cells increased along the dural venous sinus during the early postnatal period (Fig. 4, A to C, and fig. S7A). The density of CCR2$^{+}$ cells in the LM-CC was relatively low and stable, but MHCII expression in the CCR2$^{+}$ cells progressively increased, and they became CCR2$^{+}$MHCII$^{+}$ double-positive cells during the postnatal period (fig. S7, B to D). In the CP, the numbers of both CCR2$^{+}$ and MHCII$^{+}$ cells were low during the postnatal period but slowly increased from a young age (fig. S7E).

To delineate the postnatal recruitment of MHCII$^{hi}$ cells to the perisinus, we visualized MHCII and Iba1 in the perisinuses of CCR2$^{GFP/+}$ mice by immunofluorescence. In P7 neonates, most Iba1$^{+}$CCR2$^{+}$ cells were MHCII$^{-}$, but a few Iba1$^{+}$MHCII$^{+}$CCR2$^{+}$ cells were present as round and small in shape (Fig. 4D). However, in P28 young adult mice, the number of Iba1$^{+}$MHCII$^{+}$ CCR2$^{+}$ cells increased, and most of their shapes ware elongated and large (Fig. 4D). Flow cytometry analysis with WT mice confirmed that, among the CD11b$^{+}$CD64$^{+}$ macrophages, the proportion of MHCII$^{hi}$ macrophages progressively increased, whereas the proportion of CD206$^{hi}$ macrophages decreased from P7 to P28 (Fig. 4, E and F, and fig. S8A). Furthermore, Ly6C$^{+}$ monocytes increased from P7 to P28, but they did not express MHCII (fig. S8, B, D, and E). In comparison, conventional dendritic cells (cDCs) were relatively highly populated in the dura of P7 and then gradually decreased (fig. S8, C, F and G). Thus, MHCII$^{hi}$ macrophages are gradually recruited along the venous sinus at the dura as an immune barrier during the postnatal period.

To investigate mechanisms underlying the preferential recruitment of dural MHCII$^{hi}$ cells to the perisinus versus other CNS borders, we performed scRNA-seq on isolated ECs across the border tissues (fig. S9A). Through unsupervised clustering, we identified a distinct EC cluster in each CNS border region according to the expression of EC subtype–specific marker genes (fig. S9, B and C) (*31*, *32*). We selected and grouped genes related to adhesion, fenestration, or tight junctions and displayed these groups in three-dimensional (3D) scattering and violin plots. As shown in Fig. 5A and fig. S9D, dural sinus ECs were distinguished by their high expression of genes related to adhesion and fenestration and lack of expression of genes related to tight junctions. Gene ontology analysis based on differentially expressed genes (DEGs) revealed that the molecular functions of dural ECs were related to inflammatory responses, responses to pathogens, regulation of the defense response, and cell adhesion molecules. These were different from both LM-CC ECs (selective transport and maintenance of BBB) and CP ECs (protein phosphorylation and lipid metabolism) (fig. S10, A and B). Consistent with these findings, dural ECs were characterized by higher expression of adhesion molecule genes (*Vcam1*, *Icam1*, and *Selp*) and inflammatory response genes (*Cxcl10*, *Irf1*, and *Nfkbia*) (Fig. 5B). In addition, dural ECs had high expression of genes related to signaling mediators for interferon and other cytokines (*Jak1*, *Jak2*, *Irf1*, *Irf8*, *Il6st*, *Il17ra*, *Socs2*, and *Socs3*), innate

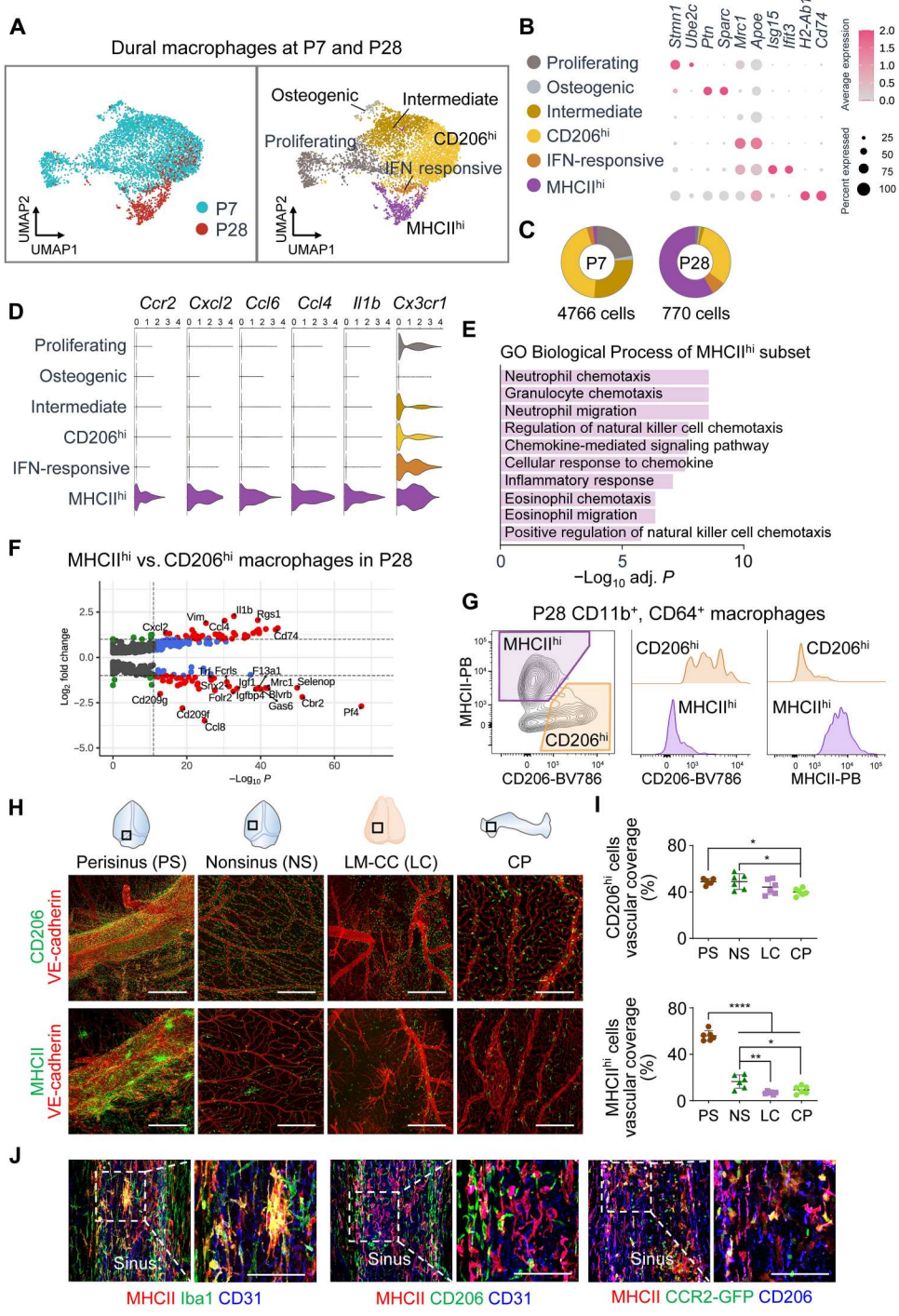


**Fig. 3. Adult mice have a distinct subpopulation of MHCII$^{hi}$ perisinus macrophages.** (**A**) UMAP plots visualizing extravascular macrophages in the dura of P7 ($n$ = 30) and P28 mice ($n$ = 30). (**B**) Dot panels depicting subsets of dural macrophages and their DEGs. (**C**) Donut plots show the fraction of each indicated cell cluster in the total number of cells of P7 (4766 cells) and P28 (770 cells) dural macrophages. (**D**) Violin plots showing normalized expressions of indicated genes in subsets of P7 and P28 dural macrophages. (**E**) Top Gene Ontology (GO) Biological Process terms based on DEGs ($log_2$ fold change > 1) between MHCII$^{hi}$ macrophages versus other macrophages. (**F**) Volcano plot displaying DEGs ($log_2$ fold change > ± 1, $-log_{10}$ $P$ > 12) between MHCII$^{hi}$ macrophages versus CD206$^{hi}$ macrophages in P28 young mice. (**G**) Flow cytometry analysis and representative histograms of MHCII$^{hi}$ and CD206$^{hi}$ macrophages. (**H** and **I**) Immunofluorescence images and comparisons of distributions of CD206$^{hi}$ and MHCII$^{hi}$ macrophages in the perisinus (PS) and nonsinus (NS) regions of the dura, LM-CC (LC), and CP of P28 young mice. Scale bars, 500 μm (perisinus, nonsinus, and LM-CC) and 200 μm (CP). The vascular coverage (%) was calculated as either total MHCII$^{+}$ or CD206$^{+}$ area divided by the total VE-cadherin$^{+}$ area. Each data point represents data from one mouse, and bars indicate mean ± SD. In (G) to (I), data are from or representative of $n$ = 6 mice per group pooled from two independent experiments. (**J**) Representative images of perisinus MHCII$^{hi}$ macrophages from P28 young mice showing that CD206 expression levels are low, but Iba1 and CCR2 are highly colocalized. Scale bars, 100 μm. Data are representative of two independent experiments with $n$ = 4 mice. $P$ values in (I) were calculated using one-way ANOVA followed by Tukey's post hoc test. *$P$ < 0.05, **$P$ < 0.01, and ****$P$ < 0.0001.

immune regulatory molecules (*Lbp*, *Fgl2*, *Csf3*, and *Cfh*), and procoagulant production (*F8* and *Serpine1*) (Fig. 5, C and D). IFS analysis confirmed that the leukocyte trafficking molecules intercellular adhesion molecule–1 (ICAM-1) and P-selectin were highly and selectively present in the ECs of the venous sinus lumen but not in ECs far from the sinus in the dura and in the LM-CC and CP without notable differences between P7 and 8-week-old mice (fig. S11, A to D). These patterns suggest that dural sinus ECs serve as sites of immune cell recruitment to the perisinus by expressing high levels of adhesion molecules for leukocyte trafficking, consistent with the emerging concept of the sinus vasculature as a strategic site for active immune-vessel cross-talk (*18*).

To address the role of high adhesion molecule levels in the postnatal recruitment of immune cells to the perisinus, we performed subcutaneous injections of blocking antibody cocktails against PSGL-1, VLA-4, and LFA-1 integrin (PVL) into P1 CC-chemokine receptor 2 (CCR2)–green fluorescent protein (GFP) neonates (Fig. 5E). ICAM-1 was high in dural sinus ECs at P1 (Fig. 5F).

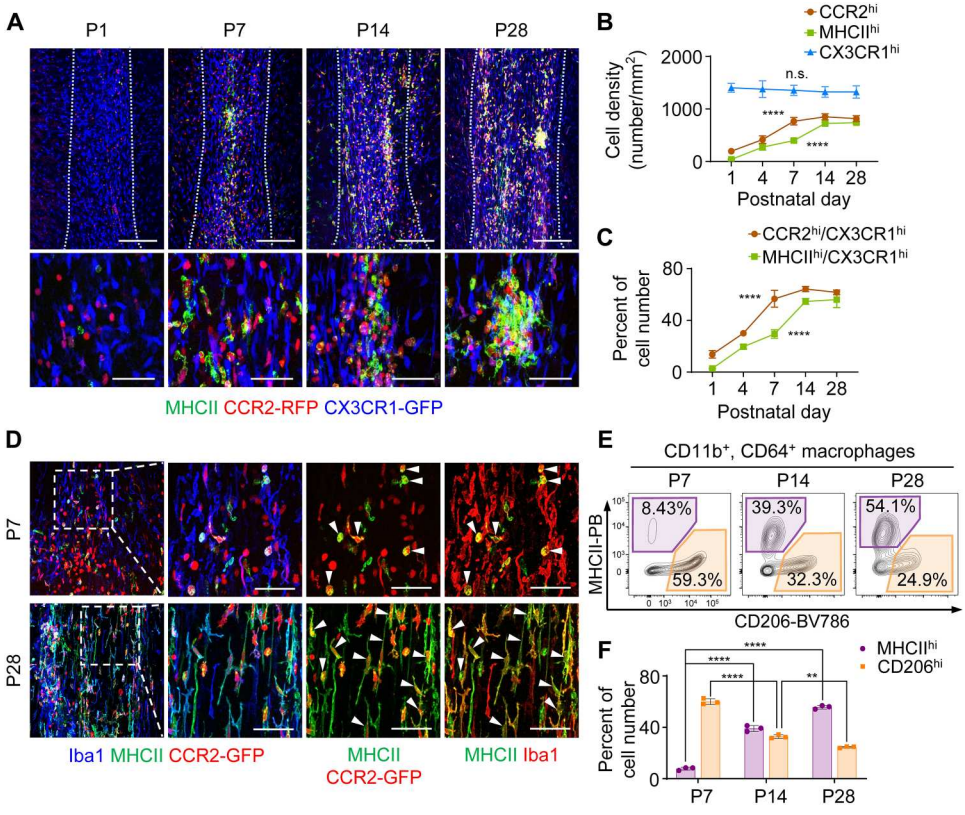


**Fig. 4. MHCII$^{hi}$ macrophages increase postnatally along venous sinuses of the dura mater.** (**A** to **C**) Immunofluorescence images and comparisons of distributions of CCR2$^{hi}$, MHCII$^{hi}$, and CX3CR1$^{hi}$ cells in the dura during postnatal development. Dotted line indicates the dural venous sinus. Scale bars, 200 μm (top) and 50 μm (bottom). Dots indicate mean ± SD. Data in (A) to (C) show or are representative of $n = 3$ mice per group pooled from two independent experiments. (**D**) Representative immunofluorescence images showing distributions of MHCII$^{hi}$ (green) and Iba1$^{+}$ (blue; red in magnified view) cells in the dura of P7 and P28 CCR2$^{GFP/+}$ mice. The dotted line box is magnified as the three right panels. Scale bars, 50 μm. Note that most MHCII$^{hi}$ cells are CCR2$^{+}$ (red) cells (white arrowheads) in both P7 and P28 mice. Data are representative of $n = 3$ mice per group pooled from two independent experiments. (**E** and **F**) Flow cytometry analysis and quantification of MHCII$^{hi}$ and CD206$^{hi}$ macrophages in P7, P14, and P28 mice. Individual data points represent data from each experiment (four to six mice pooled per group), and bars indicate mean ± SD. Data are derived from three independent experiments. Each dot indicates a mean value from four mice, and bars indicate mean ± SD. $n = 12$ mice per group from three independent experiments. *P* values in (B) and (C) were calculated by one-way ANOVA and in (F) by one-way ANOVA followed by Tukey's post hoc test. $^{**}P < 0.01$ and $^{****}P < 0.0001$.

Compared with mice treated with immunoglobulin G (IgG) at P8, PVL reduced CCR2$^{+}$ cell counts by 73% and vessel coverage of MHCII$^{+}$ cells by 91% in the perisinus (Fig. 5, G and H). However, CCR2$^{+}$ and MHCII$^{+}$ cell numbers were not reduced in CCR2-deficient (Ccr2$^{GFP/GFP}$) animals (Fig. 5, G and H), indicating that the postnatal recruitment of CCR2$^{+}$ and MHCII$^{+}$ cells was not dependent on the chemokine receptor. These findings imply that distinct endothelial characteristics of the dural venous sinus facilitate the establishment of an innate immune barrier at the dura during the postnatal period.

## Dural sinus–associated MHCII$^{hi}$ macrophages guard the CNS against systemic LCMV

The innate immune barrier at the perisinus is the initial site of contact with systemic LCMV. To uncover the roles of perisinus macrophages, we depleted them by i.c.m. injection of clodronate liposome (clodronate) (*33*) with intraperitoneal injection of PVL antibodies (clodronate + PVL) in adult mice (Fig. 6, A and B). We confirmed that the i.c.m.-injected fluorescent liposomes spatially targeted immune cells at the perisinus (Fig. 6C). Both IFS and flow cytometry analyses showed that a single clodronate treatment effectively depleted perisinus CD206$^{hi}$ macrophages, but CCR2$^{+}$ Iba1$^{+}$MHCII$^{hi}$ macrophages were rapidly recruited to the perisinus after the treatment (Fig. 6, D to G, and fig. S12, A and B). On the other hand, clodronate + PVL reduced both the numbers and proportions of MHCII$^{hi}$ and CD206$^{hi}$ macrophages in the perisinus (Fig. 6, D to G). However, cDCs were not changed in the whole dura after either clodronate or clodronate + PVL treatment (Fig. 6, F and G). After systemic LCMV injection, LCMVs and viral transcripts were abundant in the perisinuses and LM-CC of mice receiving the combination treatment, but few or none were detected in animals receiving either clodronate or PVL alone (Fig. 6, H to J). The combination of i.c.m. injection of clodronate and intraperitoneal injection of CSF1R-depleting antibody also allowed viral infection at the perisinus and LM-CC (Fig. 6I). Thus, among the cells generating innate immunity, a sustained MHCII$^{hi}$ macrophage population appears to be key to building the dural immune barrier against viral spread into the CNS early during infection. Notably, the LCMV transcript level in the spleen did not differ between PVL- and clodronate + PVL–treated mice (Fig. 6J). Collectively,

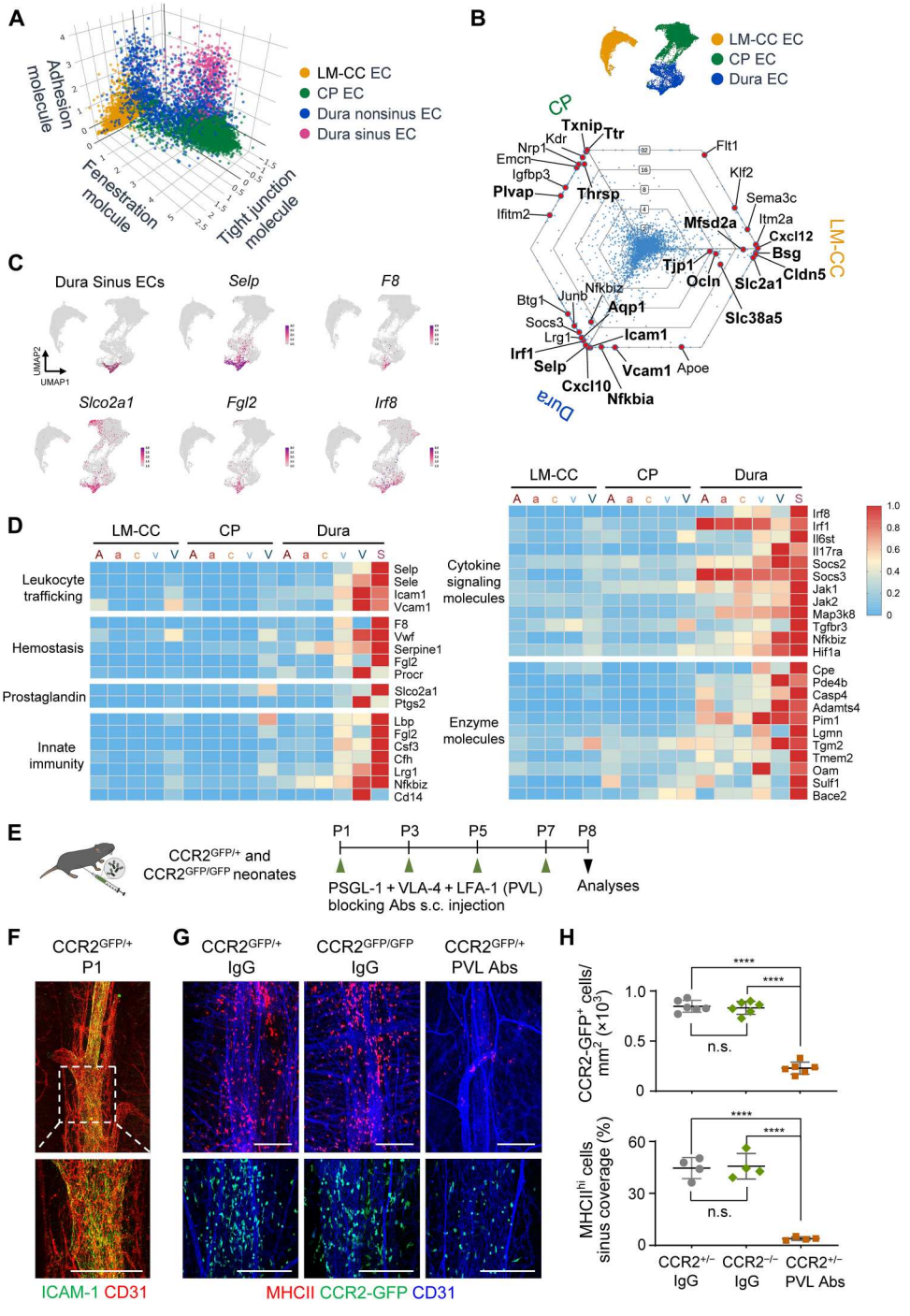


**Fig. 5. Dural venous sinus establishes an innate immune barrier during the postnatal development.** (**A**) 3D scatterplot showing differential expressions of the genes related to adhesion, fenestration, or tight junctions in each indicated EC cluster. The genes related to adhesion were *Selp*, *Sele*, *Icam1*, and *Vcam1*; fenestration was *PLVAP*; and tight junction were *Cldn5*, *Ocln*, and *Tjp1*; and the average expression was calculated as a module score. (**B**) UMAP plot and hexagonal triwise diagram depicting the indicated DEGs among the dura, LM-CC, and CP EC clusters. Longer distance from the center represents higher magnitude expression of indicated gene. (**C**) Feature plots depicting high expressions of indicated genes in the dural sinus EC subcluster. (**D**) Heatmap showing normalized expressions of dural sinus EC-specific DEGs and their molecular functions. Data in (A) to (D) are pooled from $n = 30$ mice in a single experiment. ECs from the dura (3480 cells), LM-CC (4697 cells), and CP (6612 cells) were analyzed. (**E**) Diagram depicting the experimental procedure for subcutaneous (s.c.) injection of cocktails of IgG or PVL-blocking Abs into $CCR2^{GFP/+}$ and $CCR2^{GFP/GFP}$ neonates from P1 and analyses at P8. (**F**) Images showing ICAM-1 (green) in the dural venous sinus (CD31, red) of P1 mouse. Dotted line box is magnified below. Scale bars, 200 μm. Data are representative of two independent experiments in $n = 4$ mice that show similar findings. (**G** and **H**) Images and comparisons of distributions of $CCR2^{hi}$ and $MHCII^{hi}$ cells in the dural sinus (CD31, blue) region of P8 $CCR2^{GFP/+}$ and $CCR2^{GFP/GFP}$ neonates after treatment of IgG or PVL-blocking Abs. Scale bars, 200 μm. The sinus coverage (%) was calculated as total $MHCII^{+}$ area divided by the total $CD31^{+}$ perisinus area. Individual data points represent data from one mouse, and bars indicate mean ± SD. Data show or are representative of $n = 4$ to 6 mice per group pooled from two independent experiments. *P* values in (H) were calculated using one-way ANOVA followed by Tukey's post hoc test. ****$P < 0.0001$.

these results indicate that viral propagation at the dura and LM-CC was mainly attributable to impaired local innate immune responses at the perisinus.

These findings led us to compare the molecular responses to the LCMV infection between $MHCII^{hi}$ macrophages and $CD206^{hi}$ macrophages in the dura of young adult mice. We isolated each set of macrophages from the dura at control time point (0 hours) and 12 hours after infection of systemic LCMV and performed plate-based scRNA-seq analysis (fig. S12C). Heatmap and violin plots showed that some of the up-regulated genes in the $MHCII^{hi}$ subset were classified as "cell-type intrinsic DEGs"—genes that differed from those of $CD206^{hi}$ cells regardless of their response to infection. These genes included *Cxcl16* (antiviral chemokine), *Il1b* (proinflammatory cytokine), *Csfr2a* (colony-stimulating factor receptor), *Ccr2* (C-C motif chemokine ligand 2 chemokine receptor), *Slamf7* [signaling lymphocytic activation molecule (SLAM) family—mediates stimulatory signal that promotes immune cell activation and differentiation], and *S100a11* (calcium-binding protein). The genes that were up-regulated in the $MHCII^{hi}$ subset were classified as "infection-induced DEGs"—genes that differed from those of

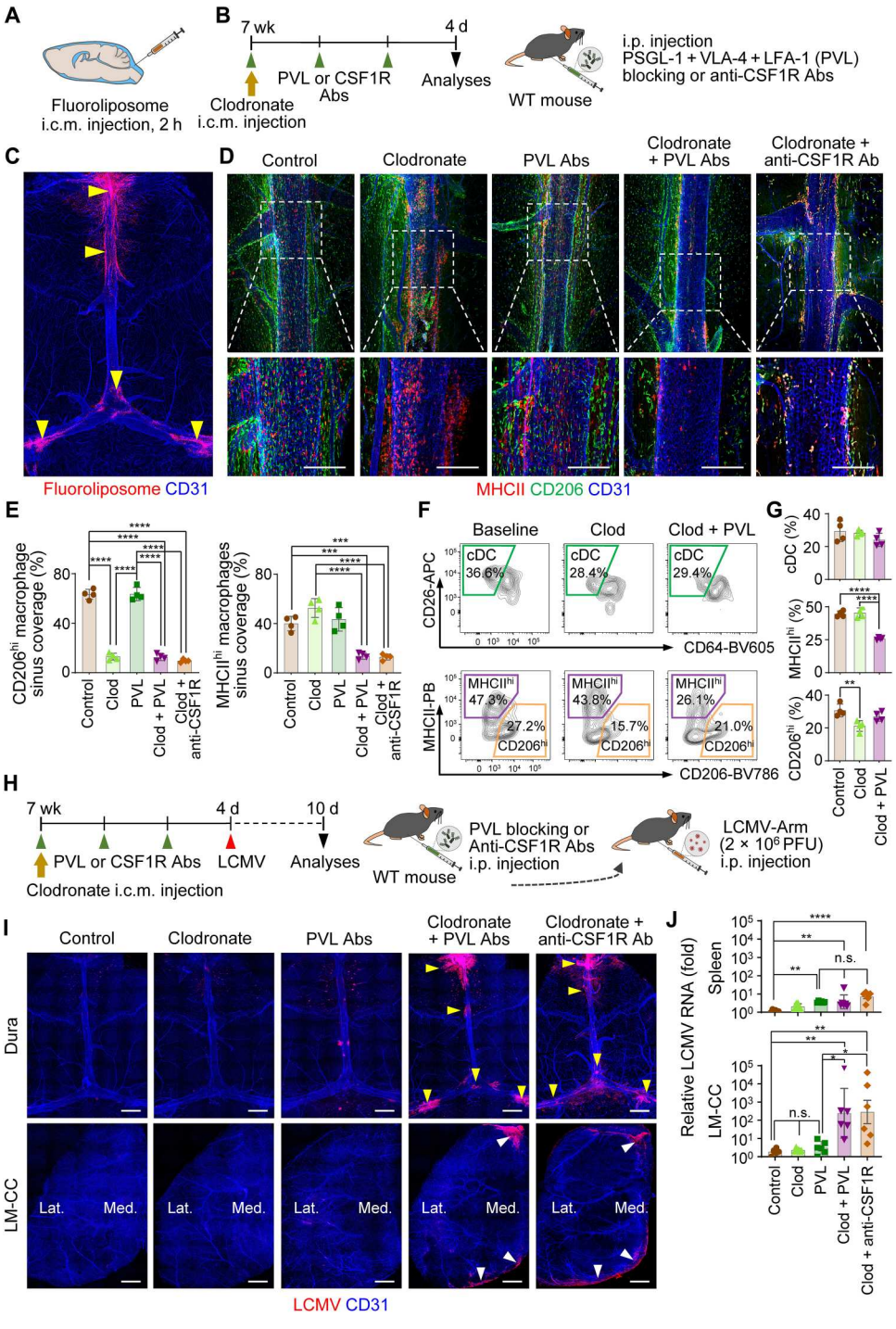


**Fig. 6. MHCII$^{hi}$ perisinus macrophages guard the CNS against systemic LCMV infection.** (**A**) Diagram depicting the experimental procedure for i.c.m. injection of fluorescent liposomes into WT B6 adult mice and analyses 2 hours later. (**B**) Diagram depicting the experimental procedure for depleting dural phagocytes. Either i.c.m. injection of control liposome (control) or clodronate liposome (Clod) followed by intraperitoneal injections of IgG or PVL-blocking Abs or anti-CSF1R–depleting Abs into adult WT B6 mice and analyses 3 days later. (**C**) Image showing uptake of liposomes (red Fluoroliposome) by perisinus (CD31, blue) phagocytes. Data are representative of two independent experiments with a total of $n = 4$ mice. (**D** and **E**) Images and comparisons for distributions of MHCII$^{hi}$ (red) or CD206$^{hi}$ (green) macrophages in the perisinus (CD31, blue) region of each indicated group. Each dotted line box is magnified below. Scale bars, 200 μm. The sinus coverage (%) was calculated as either total MHCII$^{+}$ or CD206$^{+}$ area divided by the total CD31$^{+}$ perisinus area. Individual data points represent data from one mouse, and bars indicate mean ± SD. Data in (D) and (E) show or represent $n = 4$ mice per group pooled from two independent experiments. (**F** and **G**) Flow cytometry analysis and comparisons of CD26$^{+}$ cDC, MHCII$^{hi}$, and CD206$^{hi}$ macrophages in the control group, clodronate liposome i.c.m. injection group (Clod), and clodronate liposome i.c.m. injection followed by PVL-blocking Abs intraperitoneal injection group (Clod + PVL). In (G), the proportion of cell types (%) was calculated from the parent population of either CD45$^{+}$Lin$^{-}$CD11b$^{+}$ cells (cDC) or CD45$^{+}$ Lin$^{-}$CD11b$^{+}$CD64$^{+}$ cells (MHCII$^{hi}$ or CD206$^{hi}$). Individual data points represent the results of each experiment (four to six mice pooled per group), and bars indicate mean ± SD. Data are derived from four independent experiments. (**H**) Diagram depicting the experimental procedure for i.c.m. injection of control liposome or clodronate liposome followed by intraperitoneal injection of cocktails of IgG or PVL-blocking Abs or anti-CSF1R–depleting Abs into adult WT B6 mice, and then the mice are infected with intraperitoneal injection of LCMV-Arm and analyzed 6 days later. (**I**) Immunofluorescence image of LCMV foci (red) showing that LCMV invades the perisinus (CD31, blue) region of the dura (yellow arrowheads) and the medial side of LM-CC (white arrowheads) in the Clod + PVL-blocking Abs group and Clod + anti-CSF1R–depleting Ab group. Scale bars, 1.0 mm. Data represent two independent experiments in $n = 6$ mice per group. (**J**) Comparisons of relative expression of LCMV glycoprotein RNA in the spleens and LM-CC of each indicated group. The RNA level from the control group was used as the standard group for comparison. Each data point represents data from one mouse, and bars indicate mean ± SD. Data from two independent experiments with total $n = 6$ mice per group are shown. *P* values in (E), (G), and (J) were calculated by one-way ANOVA followed by Tukey's post hoc test. $^{*}P < 0.05$, $^{**}P < 0.01$, and $^{****}P < 0.0001$.

CD206$^{hi}$ cells only in response to infection. These genes included *Klrk1* (NK cell lectin-like receptor), *Rgs1* (type I interferon–induced gene), *S100a6* and *S100a10* (calcium-binding proteins), *Slamf8* and *Slamf9* (SLAM family), and *Kcnn4* (potassium calcium–activated channel subfamily). However, in the CD206$^{hi}$ subset, the up-regulated genes were *Fcgr* (Fc gamma receptor); *Lyve1* (immune modulation); and *C1qa*, *C1qb*, and *C4b* (complement components) (fig. S12, D and F). Thus, we conclude that the resulting gene signatures provide distinct MHCII$^{hi}$ cell responses, which differ from those of CD206$^{hi}$ cells, indicating that MHCII$^{hi}$ cells contribute to antiviral responses in the dura, both through cell-intrinsic mechanisms (maintaining high transcript levels) and infection-induced mechanisms (rapidly responding to virus infection).

### The venous sinus–associated macrophage barrier protects against LCMV through a type 1 interferon–mediated signaling

To elucidate the mechanisms by which perisinus MHCII$^{hi}$ macrophages protect the CNS from systemic LCMV infection, we investigated the ability of the adaptive immune system to limit viral propagation. In WT adult mice, we noted no differences in the number and distribution of T cells after treatment with either clodronate or PVL (fig. S13, A to C). To examine whether the adaptive immune system is required for perisinus macrophages to protect against systemic LCMV, we used RAG2-deficient mice (fig. S13, A to C). Clodronate treatment in RAG2-deficient mice markedly reduced CD206$^{hi}$ macrophages but elicited no change in MHCII$^{hi}$ macrophages in the perisinus (fig. S13, D and E). After systemic LCMV injection, LCMVs and transcripts were scarce or not found in the dura and LM-CC at dpi 6 (Fig. 7, A, B, and K). These results imply that the adaptive immune system plays a minor role in limiting viral invasion into the CNS early during infection. Moreover, clodronate combined with either MHCI- or MHCII-blocking antibody did not induce any LCMV propagation into the CNS (Fig. 7, A, B, and K), suggesting that the antiviral mechanism of MHCII$^{hi}$ macrophages is neither MHCI nor MHCII dependent.

We then investigated whether cytokines secreted by perisinus MHCII$^{hi}$ macrophages could enhance antiviral barrier function. We compared changes in the expression of antiviral gene transcripts in the dura between neonates and young adult mice and between clodronate- and clodronate + PVL–treated mice at an early infection time point, 36 hours after LCMV infection (Fig. 7, C and F). Compared with neonates, young adult mice showed increased transcript levels of CCL chemokines (*Ccl4* and *Ccl5*), interferon regulatory factors (*Irf5* and *Irf7*), and other inflammatory molecules (Fig. 7D). Gene ontology analysis revealed that the up-regulated transcripts in young adult mice encoded cytokines, including granulocyte-macrophage colony-stimulating factor and interferon-α (Fig. 7E). Furthermore, compared with the clodronate + PVL group, the clodronate group showed higher expression of chemokines (*Ccl5*, *Cxcl9*, and *Cxcl10*) and proinflammatory cytokines (*Il1b* and *Il12b*) (Fig. 7, G and H). Type 1 interferon and interferon-γ signaling pathways are critical in restraining viral spread, and they nonredundantly dictate cytokine production as interferon-α/β receptor (IFNAR) dependent [e.g., interleukin-12b, CCL4, and CCL5] and interferon-γ receptor (IFNGR) dependent (e.g., CXCL9, Stat1, and Irf1) (*34*). Therefore, to delineate the downstream targets, we treated the adult mice with or without i.c.m.-injected clodronate and with either intraperitoneally injected IFNGR-blocking or IFNAR-blocking antibody (Fig. 7I). We found that IFNAR blockade but not IFNGR blockade led to viral propagation at the dura and LM-CC (Fig. 7, J and K). This implies that type 1 interferon–mediated signaling is critical for the maintenance of MHCII$^{hi}$ macrophage-dependent antiviral barriers at the perisinus, which is in line with the recent report by Rebejac *et al.* (*20*).

## DISCUSSION

Our work suggests that MHCII$^{hi}$ macrophages at the dura play a crucial role in preventing early CNS infection by activating the type 1 interferon–mediated signaling before the emergence of antigen-specific T cells. These myeloid cells are mainly located along the venous sinus of the dura and are dynamically recruited after birth. Distinct features of venous sinus ECs contribute to the preferential recruitment of immune cells and the establishment of a distinct immune barrier at the dura. Insufficient establishment of the immune barrier at the perisinus due to either immaturity (in neonates) or suppressed recruitment of MHCII$^{hi}$ macrophages is sufficient to allow LCMV entry to the CNS from the systemic circulation (fig. S14).

Our findings provide insights into the mechanism underlying neonates′ high susceptibility to viral meningoencephalitis. Because most previous observations of CNS infection have been conducted within the framework of prolonged infections, postmortem exams (*35*, *36*), or direct intracranial inoculation of pathogen models (*33*, *37*), these do not accurately represent real-world primary CNS infections (*5*, *38*). To overcome these caveats, we adopted systemic injection of LCMV for this study. LCMV is a noncytopathic virus that does not destroy CNS barrier structures and allows pathogens to be observed as they infiltrate the CNS from the periphery.

How systemic pathogens enter the CNS through its border tissues has long been debated (*1*, *5*, *39*, *40*). CNS borders constitute distinct compartments with differing accessibility to the afferent and efferent arms of the immune system (*10*). By comparing the structural components of CNS borders, we found that the perisinus is devoid of a definitive tight barrier and thus susceptible to pathogen invasion from the CSF and systemic circulation, consistent with a previous report (*18*). Moreover, our findings confirm the belief (*21*) that the route from the perisinus to the subarachnoid space is highly vulnerable as a portal to the CNS for systemic pathogens. Our findings show that LCMV infection after systemic inoculation initially takes place in the perisinus and later in the LM-CC without notable vascular leakage, supporting the "perisinus to LM-CC" route of pathogen invasion. However, this convincing concept is inconsistent with the previous view (*1*, *5*, *41*) claiming pathogen entry via the BCSFB or across the BBB into the CNS. Furthermore, there has been controversy over whether the immaturity of CNS barriers affects viral invasion of the CNS in neonates. Although one view suggests that pathogens can access the CNS through immature structural CNS barriers (*9*, *42*), the opposite view (*43*, *44*) claims the existence of a functionally competent tight barrier in neonates. Nevertheless, our findings show that the immaturity of the immune cell landscape in the dura, particularly in the perisinus region, leads to extensive LCMV propagation from the perisinus to the CNS and fatal lethality by systemic virus infection in neonates. Therefore, we

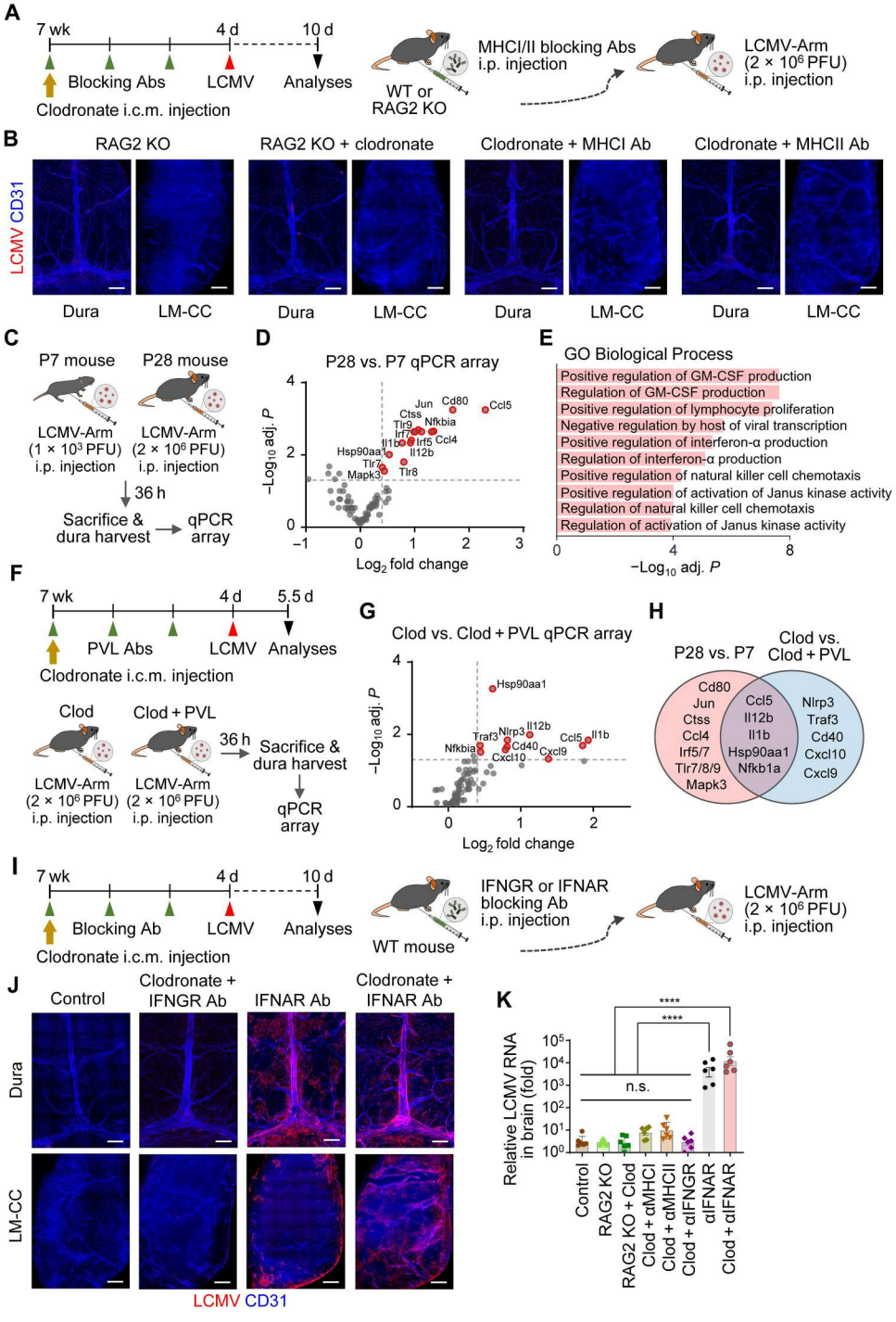


**Fig. 7. MHCII$^{hi}$ perisinus macrophage barrier protects against LCMV through a type 1 interferon–mediated signaling.** (**A**) Diagram depicting the experimental procedure for i.c.m. injection of control liposome or clodronate followed by intraperitoneal injections of cocktails of IgG or MHCI- or MHCII-blocking Abs into adult WT B6 or RAG2-deficient mice, and then the mice are infected with intraperitoneal injection of LCMV-Arm and analyzed 6 days later. (**B**) Representative immunofluorescence images showing the absence of LCMV foci (red) and blood vessels (CD31, blue) at the dura and LM-CC in both RAG2-deficient and MHCI/II blockade groups. Scale bars, 1.0 mm. Data are representative of two independent experiments with $n = 6$ mice per group. (**C**) Diagram depicting the experimental procedure for intraperitoneal injection of the weight-adjusted amount of LCMV-Arm into P7 and P28 B6 mice and harvest of dura at 36 hours after injection followed by qPCR array analysis. (**D**) Volcano plot displaying DEGs ($\log_2$ fold change > 0.4, $-\log_{10}$ adj. $P > 1.3$) between P28 versus P7 dura. (**E**) Top GO Biological Process terms based on DEGs ($\log_2$ fold change > 0.75, $-\log_{10}P > 3$) between P28 versus P7 dura. GM-CSF, granulocyte-macrophage colony-stimulating factor. (**F**) Diagram depicting the experimental procedure for intraperitoneal injection of LCMV-Arm into the clodronate injection group (Clod) and clodronate + PVL-blocking Abs injection group (Clod + PVL) and harvest of dura at 36 hours after injection followed by qPCR array analysis. (**G**) Volcano plot displaying DEGs ($\log_2$ fold change > 0.4, $-\log_{10}$ adj. $P > 1.3$) between Clod versus Clod + PVL dura. (**H**) Venn diagram displaying DEGs that are distinct and shared between P28 versus P7 or Clod versus Clod + PVL. In (C) to (H), data are from or representative of $n = 10$ mice per group for each experiment, from four independent experiments. (**I**) Diagram depicting the experimental procedure for i.c.m. injection of control liposome or clodronate followed by intraperitoneal injection of IgG, anti-IFNAR–blocking Ab, or anti-IFNGR–blocking Ab into adult WT B6 mice, and then the mice are infected with intraperitoneal injection of LCMV-Arm and analyzed 6 days later. (**J**) Immunofluorescence images showing LCMV foci (red) and blood vessels (CD31, blue) at the dura and LM-CC in indicated groups. Note that the clodronate + IFNAR–blocking Ab group or only IFNAR-blocking Ab group shows LCMV foci in the dura and LM-CC. Scale bars, 1.0 mm. Data represent two independent experiments with $n = 6$ mice per group. (**K**) Comparison of relative expression of LCMV glycoprotein RNA in the LM-CC of each indicated group. The lowest value of RNA expression among samples, based on threshold cycles ($2^{-\Delta\Delta Ct}$) of RT-PCR, was used as the standard for fold comparisons. Each data point represents data from an individual mouse, and bars indicate mean ± SD. Data show $n = 6$ mice per group pooled from two independent experiments. *P* values in (K) were calculated by one-way ANOVA followed by Tukey's post hoc test. ****$P < 0.0001$.

propose that the immaturity of the perivenous sinus immune barrier is a key factor in neonates' high susceptibility to viral meningoencephalitis.

We identified MHCII$^{hi}$ macrophages along the venous sinus at the dura as providing protection within the CNS against systemic LCMV infection. These cells are CD206 negative or CD206 low and are recruited from circulating blood in a leukocyte adhesion molecule–dependent manner not only in both neonates and adults. The perisinus immune barrier constituted by these MHCII$^{hi}$ macrophages seems equipped with constitutive type 1 interferon–mediated signaling. Moreover, neither RAG2-deficient mice nor WT mice treated with the MHCII blockade showed impairment of the immune barrier against LCMV propagation from the perisinus to the CNS, suggesting that adaptive immune cells play a minor protective role, at least in the early infection period. Hence, it would be interesting to examine the role of MHCII$^{hi}$ macrophages at the perisinus to protect the CNS against systemic infection of *T. brucei*, a cytopathic parasite that destroys CNS barrier structures (*24*).

A recent study (*20*) reports that MHCII$^{+}$CD206$^{hi}$ macrophages, extensively and evenly distributed across dura, protect the CNS against infection by neurotropic viruses. However, the MHCII$^{hi}$ macrophage subpopulation we identified in this study differs from the MHCII$^{+}$CD206$^{hi}$ macrophage subpopulation in regard to its preferential localization, shaping the venous sinus–associated barrier, formation of a protective immune barrier against virus invasion, molecular profile, recruitment mode, and its link to neonatal susceptibility to meningoencephalitis.

In summary, our study reveals that in systemic viral infection, immaturity of the perisinus innate immune barrier constituted mainly by MHCII$^{hi}$ macrophages allows virus entry to the CNS from the dura, causing fatal meningoencephalitis in neonatal mice. Establishing and maintaining the perisinus innate immune barrier is key to preventing virus-induced meningitis and CNS infections.

## MATERIALS AND METHODS

### Study design

This study aimed to determine the structural and functional differences among the CNS borders to understand the immunosurveillance mechanisms that protect normal adult mice, including 4-week-old (young adult) and 8-week-old adult mice, but not P7 neonates, against virus-mediated meningitis. We used the systemic LCMV infection model, which does not destroy CNS barriers, and used immunofluorescence to evaluate CNS structures; fluorescent-OVA tracing to evaluate barrier function; scRNA-seq analyses and flow cytometry to characterize immune and endothelial cells; blocking antibodies or diphtheria toxin to deplete specific immune cells populations in the CNS borders of mice; and blocking antibodies or/and clodronate to examine macrophage recruited to the perisinus in neonates. Similar ages of adult male mice were assigned randomly to the experiment groups. For neonates, we used both male and female mice. The samples we used for experiments were unblinded throughout quantification and analysis.

### Study approval

The experiments on the mice were conducted according to the approval (KA2020-78 and KA2020-79) of the Animal Care Committee of the Korea Advanced Institute of Science and Technology (KAIST).

### Mice

C57BL/6J, Ccr2$^{RFP}$Cx3cr1$^{GFP}$ dual-reporter mice [B6.129(Cg)-*Cx3cr1*$^{tm1Litt}$ *Ccr2*$^{tm2.1Ifc}$/JernJ, #032127], *Ccr2*-GFP knock-in mice [B6(C)-*Ccr2*$^{tm1.1Cln}$/J, #027619], and CXCL12-dsRed mice (*Cxcl12tm2.1Sjm*/J, #022458) were obtained from the Jackson Laboratory. RAG2-deficient (C57BL/6 N-*Rag2*$^{tm1/Ciphe}$*Rj*) mice were purchased from Janvier Labs (Le Genest-Saint-Isle, France). CX3CR1-DTR mice (*45*) were obtained from K. Soon Kim and C. D. Surh (Academy of Immunology and Microbiology, IBS/POSTECH, Pohang, Republic of Korea) and transferred and bred in our animal facilities. All mouse strains were bred and maintained under specific pathogen–free conditions at KAIST. Mice were anesthetized with intraperitoneal injection of a combination of anesthetics (80 mg/kg of ketamine and 8 mg/kg of xylazine) before all experiments or being sacrificed.

### Administrations of Fluor-OVA via three routes

For adult mice, 50 μl (2 mg/ml) of Alexa Fluor 488–conjugated ovalbumin (Fluor-OVA) was intravenously administered via the retro-orbital route. For neonatal mice, 15 μl (5 mg/ml) of Fluor-OVA was intraperitoneally administered. For i.c.m. administration, the necks of adult mice were shaved, cleaned with 70% ethanol, and laid prone on a stereotaxic frame under a microscope. As previously reported (*46*), the head was adjusted to a 90° angle to the body axis to facilitate access to the cisterna magna. After a skin incision to the midline of the posterior neck, muscle layers were carefully separated with microretractors. The atlantooccipital membrane overlying the cisterna magna was superficially penetrated using a 33-gauge NanoFil needle (World Precision Instruments). Then, 3 μl (5 mg/ml) of Fluor-OVA was infused into the subarachnoid space at 1 μl/min for 3 min using a syringe pump (Chemyx). The needle was slowly removed after the mouse was left in the position for 5 min to prevent CSF leakage. The muscle layers and neck skin were then sutured with black silk.

For intracerebroventricular injection, a small hole was drilled at the medial-lateral axis 1 mm and anterior-posterior axis −0.5 mm relative to the bregma after the skull exposure on a stereotaxic frame. A 30-gauge NanoFil needle (World Precision Instrument) connected to a PE-20 catheter was inserted to a depth of 2.2 mm. A total of 2.5 μl of phosphate-buffered saline (PBS) containing Flour-OVA (5 mg/ml) was infused into the ventricle at a 1 μl/min rate for 2.5 min using a microsyringe (88000, Hamilton) and a microinfusion machine (Fusion 100, Chemyx Inc.). After infusion, the NanoFil needle was left in place for 5 min to prevent backflow and then slowly removed. The hole was sealed with a mixture of super glue and resin. The mice were sacrificed 30 min after intravenous injection, intracerebroventricular injection (for adult mice), or intraperitoneal injection (for P7 pups) and 2 hours after i.c.m. injection to trace administered Fluor-OVA at the CNS borders.

### LCMV inoculation

To induce acute meningitis, mice at the indicated age were infected with LCMV Armstrong (LCMV-Arm) (*47*, *48*), a gift from S.-J. Ha (Yonsei University, Korea). LCMV stocks were prepared by infecting BHK-21 cells and harvesting the supernatant at 72 hours after infection. Viral titers were determined by plaque formation on Vero

cells. All experiments involving LCMV were carried out at biosafety level 2. To observe CNS pathogen entry patterns, LCMV was administered either intraperitoneally (100 μl for adults and 10 μl for neonates) or i.c.m. (3 μl for adults, 1 μl/min for 3 min using a syringe pump). After the injection of viruses, survival was monitored daily.

### In vivo dural immune cell depletion

All antibodies used for the following experiments were purchased from Bio X Cell (data file S1). For the neonatal mice, a cocktail of 100 μg of each rat anti-mouse PSGL-1 (clone 4RA10), VLA-4 (clone PS/2), and LFA-1 antibody (clone M17/4) was injected subcutaneously every other day from P1 until the sampling time point. The control group mice were given cocktails of the same dose of rat anti-mouse IgG1 isotype (clone HRPN), rat anti-mouse IgG2b isotype (clone LTF-2), and rat anti-mouse IgG2a isotype (clone 2A3) in the same manner. For depleting experiments in adult mice, a cocktail of 400 μg each of rat anti-mouse CD90.2 (clone 30H12), Gr-1 (clone RB6-8C5), c-Kit (clone ACK2), PDCA-1 (clone 927), and NK1.1 (clone PK136) was intraperitoneally injected for three consecutive days. The control group mice were given the same dose of rat anti-mouse IgG2a isotype. For Csf1r depletion, 400 μg of rat anti-mouse Csf1r (clone AFS98) was intraperitoneally injected on days 1, 2, and 3 after i.c.m. injection of clodronate liposome. For the experiment targeting the perisinus, cocktails of 250 μg each of rat anti-mouse PSGL-1, VLA-4, and LFA-1 antibody were intraperitoneally injected every day on days 1, 2, and 3 after i.c.m. injection of clodronate liposome. The control group mice were given the same dose of rat anti-mouse IgG1 isotype, rat anti-mouse IgG2b isotype, and rat anti-mouse IgG2a isotype in the same manner. To deplete dural phagocytic cells, 5 μl of clodronate liposome or control liposome (CLD-8901, Encapsula NanoSciences) was injected i.c.m. at 1 μl/min for 5 min using a syringe pump (Chemyx). The same volume of Fluoroliposome (CLD-8911, Encapsula NanoSciences) was injected i.c.m. to observe the spatial distribution of liposome. For the blocking experiment, 400 μg of rat anti-mouse MHCII (clone M5/114), IFNAR-1 (clone MAR1-5A3), and IFNGR (clone GR-20) was injected subcutaneously on days 1, 2, and 3 after i.c.m. injection of clodronate liposome. For MHCI blocking, a combination of 200 μg of each rat anti-mouse MHCI (H-2Kd, clone SF1.1.10) and MHCI (H-Kk, H-2Dk, clone 15-3-1S) was injected after i.c.m. injection of clodronate liposome.

### Diphtheria toxin treatment for CX3CR1-DTR mice

To deplete macrophages at the dura, $CX3CR1^{DTR}$ mice or WT mice were intraperitoneally injected with 600 ng of diphtheria toxin (D0564, Sigma-Aldrich) dissolved in 150 μl of PBS for three consecutive days. One day after the last injection, the LCMV was injected intraperitoneally.

### Sample preparations for histological analyses

Mice were perfused with ice-cold PBS followed by 4% paraformaldehyde (PFA) through the left ventricle by puncturing the right auricle. For a sampling of meninges in a whole-mounted or cryosectioned, the covering skin and neck muscles were stripped, and the mandible and brain were removed from the skull. Then, the dorsal part of the skull was dissected as previously described (*49*). An incision was made from the cisterna magna along the suture lines of the skull parietal bone until the rostral part was reached on both sides, and the parietal bone containing meninges was dissected. The whole-mounted skull bearing dura was then fixed with 2% PFA for 2 hours at 4°C and decalcified with 0.5 M EDTA (pH 7.4) at 4°C for a day. For cryo-section of the calvaria, the dissected part of the skull was fixed with 2% PFA for 3 hours at 4°C and decalcified with 0.5 M EDTA (pH 7.4) at 4°C for a day, embedded and frozen in a frozen section medium (Leica) without dehydration, and cut into 12-μm sections using Cryocut Microtome (Leica). The brain was isolated for the preparation of the LM-CC, and incisions were made along the longitudinal fissure to cut cerebral hemispheres in half. The olfactory bulb and cerebellum were removed with a scalpel knife. An additional incision was made along the anterior and posterior corpus callosum level to obtain leptomeninges and attached dorsal brain cortical region. The dissected LM-CC was fixed with 2% PFA for 2 hours at 4°C. For the brain parenchyma section, the dissected brain was fixed with 4% PFA for 4 hours at 4°C, cut into a 100-μm-thick coronal section using a vibrating microtome (VT1200S, Leica), and postfixed with 4% PFA for 30 min at 4°C. For whole-mount staining of CP in the lateral ventricle (LV), cerebral cortical hemispheres were separated, and incisions were made along the anterior and posterior fornix to expose CP from LV space according to the previous report (*50*). Then, CP was detached from the hippocampus using fine forceps, and dissected CP was fixed with 2% PFA for 2 hours at 4°C.

### IFS and imaging

For IFS, samples were permeabilized and blocked with a blocking buffer containing 5% donkey or goat serum in 1% Triton X-100/1× PBS for 1 hour at room temperature. For the samples treated with the PVL-blocking antibodies or their respective isotype control antibodies, additional blocking with AffiniPure Fab Fragment donkey anti-rat IgG (100 μg/ml) (712-007-003, Jackson ImmunoResearch) in PBS was performed for 2 hours at room temperature. Samples were then incubated overnight at 4°C with the following primary antibodies (1:400 dilution): anti-LCMV (clone VL-4), anti-ICAM1 (clone YN1/1.7.4; all antibodies were from Bio X Cell), anti-CD31 (clone 2H8, Merck), anti-vimentin (chicken polyclonal, Millipore), anti–vascular endothelial (VE)–cadherin (goat polyclonal), anti–E-cadherin (goat polyclonal; all antibodies were from R&D Systems), anti–claudin-5 (rabbit polyclonal), anti–ZO-1 (rabbit polyclonal), anti-MHCII (clone M5/114.15.2; all antibodies were from Invitrogen); anti-Iba1 (rabbit polyclonal, Wako), anti–P-selectin (clone RB40.34), anti-plasmalemma vesicle-associated protein (PLVAP) (clone MECA-32), anti-B220 (clone RA3-6B2), anti-CD3e (clone 145-2C11; all antibodies were from BD Biosciences), anti-CD206 (rabbit polyclonal), anti-Ki67 (clone SP6; all antibodies were from Abcam), and anti-CD11c (D1V9Y, Cell Signaling Technology). Please see data file S1 for further information about the antibodies. Then, the samples were washed and incubated for 3 hours at room temperature with Alexa Fluor 488–, Alexa Fluor 594–, or Alexa Fluor 647–conjugated secondary antibodies (1:1000 dilution) purchased from Jackson ImmunoResearch. Nuclei were stained with 4′,6-diamidino-2-phenylindole (DAPI; 1:1000 dilution, Invitrogen). The samples were then mounted with a fluorescent mounting medium (VECTASHIELD), and immunofluorescent images were acquired using an LSM 800 or LSM 880 confocal microscope (Carl Zeiss). ZEN 2.3 software (Carl Zeiss) was used to acquire and process images. Confocal images of

whole-mount samples were maximum intensity projections of tiled *z*-stack images taken at the optimal interval through the entire thickness of tissues with the following objectives: air objectives Plan-Apochromat 10×/0.45 numerical aperture (NA) M27 and Plan-Apochromat 20×/0.8 NA M27; water objectives C-Apochromat 40×/1.20 NA water immersion Corr (LSM 800) and LD C-Apochromat 40×/1.1 NA water immersion Corr M27 (LSM 880) with multichannel scanning in the frame. 3D reconstruction images were created from *z*-stack confocal images using the 3D tab in ZEN 2.3 software.

### Morphometric analyses

Quantification was performed using the maximum intensity projection images. Image analysis was done using Fiji software (National Institutes of Health). The number of CNS border immune cells was quantified by thresholding the positive signals and analyzing particles in five random 1.0 $mm^2$ fields per sample. The LCMV nucleoprotein-positive area was measured in the total area of whole-mount dura, LM-CC, and LV CP samples. For the measurement of perisinus cell numbers and sinus coverage, the perisinus was defined as a superior sagittal sinus region approximately 1 mm anterior from the confluence of the sinuses region and 1 mm posterior to the bregma point of the skull. The sinus coverage of $MHCII^+$ or $CD206^+$ macrophages was defined as the total $MHCII^+$ or $CD206^+$ area divided by the total $CD31^+$ area of the perisinus. The vessel coverage of $MHCII^+$ or $CD206^+$ macrophages was defined as the total $MHCII^+$ or $CD206^+$ area divided by the total VE-cadherin$^+$ area in five random 1-$mm^2$ fields per sample.

### Quantitative real-time RT-PCR

For RNA extraction, samples were homogenized in TRIzol solution (15596026, Invitrogen) with a Precellys 24 tissue homogenizer (Bertin Technologies) and extracted according to the manufacturer's instructions. Total RNA was reverse-transcribed into cDNA using SuperScript IV VILO Master mix with an ezDNase Enzyme kit (11766050, Invitrogen). Then, quantitative real-time PCR was conducted using the FastStart Sybr Green Master Mix (Roche) and QuantStudio 5 Real-Time PCR System (Applied Biosystems). Primers for LCMV viral load measurement were designed according to the previous report (*51*). Glyceraldehyde-3-phosphate dehydrogenase was used as a reference gene. PCR primer sequences are as follows: LCMV-Arm glycoprotein, CATTCACCTGGACTTTG TCAGACTC (forward) and GCAACTGCTGTGTTCCCGAAAC (reverse); and *Gapdh*, CATCACTGCCACCCAGAAGACTG (forward) and ATGCCAGTGAGCTTCCCGTTCAG. The follow ing cycling conditions were used: an initial denaturation step of 9 5°C for 10 min followed by 40 cycles of 95°C for 5 s and 65°C for 30 s. Reactions were performed in triplicate, and postamplification melting curve analysis was performed to ensure reaction specificity.

### Real-time PCR arrays

RNA was extracted from the homogenized samples and purified using the RNeasy Plus Mini Kit (74134, Qiagen). Total RNA was reverse-transcribed into cDNA using the RT2 First Strand Kit (330404, Qiagen) with 0.5 μg of RNA per sample. The cDNA was loaded on an Antiviral Response quantitative PCR (qPCR) array (330231 PAMM-122ZA, Qiagen), which profiles 84 standardized gene transcripts involved in the innate antiviral immune response and five reference genes, and quantitative real-time PCR was conducted using the QuantStudio 5 Real-Time PCR System (Applied Biosystems) according to the manufacturer's instructions.

### Single-cell dissociation

The dural meninges, CP, brain, and deep cervical lymph nodes (dcLNs) were sampled from the indicated mice. Meningeal layers containing dura, CP in LV and fourth ventricle (by separating cerebellum and pons), leptomeninges and attached dorsal brain cortical regions (LM-CC), and dcLNs were isolated as described for the histological analyses and placed in an ice-cold RPMI 1640 medium (22400089, Gibco). Isolated samples were digested with enzyme buffer containing collagenase type IV (2 mg/ml; 17104019, Gibco), deoxyribonuclease I (0.1 mg/ml; 10104159001, Roche) at 37°C for 30 min, and neutralized with complete medium. For the following steps, samples were kept on ice. Samples were then filtered with a 70-μm nylon mesh strainer to remove cell clumps, and the filtered samples were washed twice with ice-cold PBS and centrifugation at 500*g*, 8 min at 4°C. For LM-CC, washed samples were mixed 1:1 (v/v) with 22% bovine serum albumin in 1× PBS to remove myelin, and then the mixture was centrifuged at 1000*g*, 10 min at 4°C. The myelin layer on top of the tube was carefully removed, and the pellets were transferred to a fresh tube and washed twice with ice-cold PBS. After washing, samples were resuspended in ice-cold PBS.

### Flow cytometry analysis

Dead cells were excluded from analysis by staining with Ghost Dye Violet 510 (#13-0870-T500, Tonbo). Single suspended cells were blocked with anti-mouse CD16/CD32 (553142, BD Biosciences), and extracellular staining was performed in fluorescence-activated cell sorting (FACS) buffer (2% fetal bovine serum in PBS) with the following antibodies at 1:100 dilution: phycoerythrin (PE) anti-mouse CD206 (clone MR6F3), fluorescein isothiocyanate (FITC) anti-mouse CD45 (clone 30-F11), peridinin-chlorophyll-protein (PerCP)/Cyanine5.5 anti-mouse T cell receptor β (clone H57-597), allophycocyanin (APC) anti-mouse CD31 (clone MEC13.3), PE anti-mouse Ly6C (clone AL-21), APC/cyanine7 anti-mouse CD45.2 (clone 104), APC/cyanine7 anti-mouse CD11b (clone M1/70), PE anti-mouse CD11b (clone M1/70), APC anti-mouse CD11b (clone M1/70), PerCP/Cyanine5.5 anti-mouse CD11b (clone M1/70), PerCP/Cyanine5.5 anti-mouse Ly-6G (clone 1A8), Pacific Blue anti-mouse Ly-6G (clone 1A8), PE/Cy7 anti-mouse Gr-1 (clone RB6-8C5), PerCP/Cyanine5.5 anti-mouse NK1.1 (clone PK136), BV605 anti-mouse NK1.1 (clone PK136), PerCP/Cyanine5.5 anti-mouse CD19 (clone 1D3/CD19), PE/Cy7 anti-mouse CD19 (clone 6D5), PerCP/Cyanine5.5 anti-mouse CD3e (clone 145-2C11), PerCP/Cyanine5.5 anti-mouse lymphocyte antigen 76 (clone TER-119), PE anti-mouse CD4 (clone GK1.5), APC anti-mouse CD8 (clone 53-6.7), Pacific Blue anti-mouse I-A/I-E (clone M5/114.15.2), PerCP/Cyanine5.5 anti-mouse Ly6C (clone HK1.4), PE/Cy7 anti-mouse Ly6C (clone HK1.4), BV605 anti-mouse Ly6C (clone HK1.4), PE/Cy7 anti-mouse CD11c (clone N418), APC anti-mouse CD26 (clone H194-112), BV605 anti-mouse CD64 (clone X54-5/7.1), BV785 anti-mouse CD206 (clone C068C2), PE PDCA-1 (clone 927), APC anti-mouse ST2 (clone DIH9), PE anti-mouse CD127 (clone A7R34), Pacific Blue anti-mouse CD25 (clone PC61), PE/Cy7 anti-mouse CD49b (clone DX5), APC anti-mouse CD117 (clone ACK2), Pacific Blue anti-mouse FceRIa (clone MAR-1), or Pacific Blue anti-mouse I-

A/I-E (clone M5/114.15.2). Please see data file S1 for further information about the antibodies. Data were obtained with FACS Aria II (BD Biosciences) and analyzed using FlowJo v10 (Tree Star Inc., Ashland, OR) software.

### Droplet-based scRNA-seq

For EC scRNA-seq of the CNS borders, FACS-sorted live singlet ECs (singlet$^+$live$^+$CD45$^-$CD31$^+$) were collected from 30 adult mice. For scRNA-seq of extravascular CD45$^+$ cells of the dura, intravascular CD45$^+$ cells were labeled by intracardiac injection of anti–CD45-FITC antibody (11-0451-85, 30-F11, Invitrogen) for 30 s followed by intracardiac perfusion with ice-cold PBS to 30 P7 and 30 P28 B6 mice. Then, the dura was harvested, and single cells were collected according to the single-cell dissociation methods. Leukocytes were gated with anti-CD45-APC/cyanine7 antibody (109824, 104, BioLegend), and 4850 (P7) and 4761 cells (P28) singlet$^+$live$^+$CD45$^+$CD45iv$^-$ cells were collected. The collected live cells were suspended in 2% fetal bovine serum/PBS buffer and processed by 10× Chromium Single-cell 3′ Reagent Kit v3 (10X Genomics) according to the manufacturer's protocols. Briefly, cells were mixed with reverse-transcription reagent mix and primer and loaded to 10× chips. Cells were separated into gel beads in emulsion, where transcripts from individual cells were uniquely barcoded. Barcoded transcripts were directly reverse-transcribed and amplified to produce cDNA libraries. Size selection of the initial cDNA libraries was performed using SPRI beads (Beckman Coulter). Then, the adaptors were ligated and amplified by sample-index PCR. After another round of double-sided size selection, the quality of the final library was checked by Agilent Bioanalyzer High Sensitivity Chip. Libraries that passed the final quality control were sequenced by the Illumina HiSeq-X platform.

### Plate-based scRNA-seq (Smart-Seq3)

For plate-based scRNA-seq of the macrophages, MHCII$^{hi}$ and CD206$^{hi}$ macrophage populations (singlet$^+$live$^+$ivCD45$^-$CD45$^+$Lin$^+$CD11b$^+$CD64$^+$) were sorted and collected from 15 to 20 P28 mice. The live single cells were sorted directly to each well in a 96-well plate containing the lysis buffer. After sorting, plates were snap-frozen in liquid nitrogen and stored in a −80°C deep freezer. Plate-based single-cell libraries were generated following the Smart-Seq3 protocol (*52*). Briefly, cells were lysed, and mRNAs were reverse-transcribed. cDNAs were amplified and purified using Ampure XP beads (Beckman Coulter). Purified cDNAs were diluted to 100 pg/μl and tagmented using a Tn5 tagmentation mix (Illumina). Tagmented products were amplified with custom index primers and pooled into a single tube. After final cleanup using Ampure XP beads, resulting libraries were analyzed by tape station for quality control. The Illumina Hiseq-X platform sequenced libraries passing the quality control.

### Preprocessing of single-cell data

For droplet-based sequencing, sequenced libraries were demultiplexed and aligned to the mouse reference genome (mm10) by cellranger (version 3.0.2). Then, the aligned reads were merged to produce a raw read count matrix by featureCount function in the Subread package. Raw expression matrices were constructed using the Read10X function in the R package Seurat (version 3.1.1). Before clustering analysis, low-quality cells detected with fewer than 500 genes, and putative dead cells with high mitochondrial percentages (>10% of reads mapped to mitochondrial genes) were discarded. Cells with more than twice the median of detected gene numbers were considered as doublets and removed. For gene-based quality control, genes detected in fewer than three cells were removed from the raw expression matrix. After such quality control of unwanted cells and genes, expression matrices were normalized column-wise, dividing each gene′s unique molecular identifier (UMI) counts by the sum of UMI counts for a given cell. Then, scale factor 10,000 was multiplied, and $\log_2$ was transformed to yield log counts per million equivalent values.

For plate-based sequencing, sequenced libraries were demultiplexed and aligned to mouse reference genome (mm10) by STAR (version 2.7.9.a). Next, the featureCount (version 2.0.1) function from the Subread package was used to merge the aligned files and to create raw read count matrices. Quality control was performed by discarding cells with fewer than 1000 genes detected or more than 10% of total reads mapped to mitochondrial genes, because they were considered low-quality/dead cells. At the gene level, genes expressed in fewer than three cells were removed from the expression matrix.

### Clustering analysis

Clustering and downstream analysis were performed by the R package Seurat. The top 2000 most variable genes for each dataset were identified by the FindVariableFeatures function with options: selection.method = "vst." To reduce the effect of dissociation-induced genes on reduction and clustering, we removed a previously described list of dissociation-induced genes (*53*) from the highly variable gene list. For initial dimensionality reduction, principal components analysis was performed. The top 20 principal components were selected for further downstream analysis such as Uniform Manifold Approximation and Projection (UMAP) for 2D visualization and shared nearest neighborhood graph for neighborhood detection and cluster identification using the Louvain algorithm. For the EC datasets, after initial clustering, a small number of contaminating non-ECs [e.g., CD45$^+$ immune cells, platelet-derived growth factor receptor alpha (PDGFRα)$^+$ stromal cells, E-cadherin$^+$ epithelial cells, and others] were removed. The remaining CD31$^+$/VE-cadherin$^+$ ECs were dimensionality-reduced and clustered again as described above. For the CD45$^+$ datasets, a small number of contaminating nonimmune cells (e.g., PDGFRα$^+$ stromal cells, E-cadherin$^+$ epithelial cells, endothelial cells, and others) and Tmem119$^+$ microglia were removed. For identification of DEGs across the clusters, the FindMarkers function in Seurat was used with options: test.use = "MAST," min.pct = 0.3, and logfc.-threshold = 0.3. For comparing CD206$^{hi}$ and MHCII$^{hi}$ macrophages, intersection of DEGs between two subtypes at control time point (0 hours) and 12 hours after the LCMV infection (12 hours) was defined as cell-type intrinsic DEGs. The relative complement of DEGs at 0 hours in DEGs at 12 hours were defined as infection-induced DEGs.

### Integration of datasets

For integrative analysis of datasets showing substantial batch effects, integration functions in Seurat were used. Two thousand genes with the highest median variability across datasets were determined by the SelectIntegrationFeatures function. Then, the FindIntegrationAnchors function was used to identify anchors before integration. Last, datasets were integrated using the IntegrateData function.

Dimensionality reduction and cluster identification were performed using the integrated assay for visualization.

### Comparing gene expression and molecular function among the CNS borders

To analyze and visualize the gene expression difference among dura, LM-CC, and CP, the triwise package (https://github.com/saeyslab/triwise) was used. Gene ontology enrichment analysis on the cluster markers was performed using the g:Profiler web toolset. DEGs with at least a twofold change in expression were selected as cluster markers. Gene ontology terms adjusted to $P < 0.05$ in the biological process or Kyoto Encyclopedia of Genes and Genomes pathway categories were selected.

### Statistical analyses

Statistical significance was determined with one-way analysis of variance (ANOVA) followed by Tukey's post hoc test to test the differences between more than two groups or the time-dependent differences in one group. For the test comparing two independent variables (time and group), two-way ANOVA followed by Tukey's post hoc test was used. For qPCR array analysis, multiple unpaired *t* test with false discovery rate correction by two-stage step-up method of Benjamini, Krieger, and Yekutieli was used. Statistical analysis was performed with Prism 9 (GraphPad).

## Supplementary Materials

**This PDF file includes:**
Figs. S1 to S14

**Other Supplementary Material for this manuscript includes the following:**
Data files S1 and S2
MDAR Reproducibility Checklist

## REFERENCES AND NOTES


1. M. D. Cain, H. Salimi, M. S. Diamond, R. S. Klein, Mechanisms of pathogen invasion into the central nervous system. *Neuron* **103**, 771–783 (2019).
2. B. Engelhardt, C. Coisne, Fluids and barriers of the CNS establish immune privilege by confining immune surveillance to a two-walled *castle moat* surrounding the CNS castle. *Fluids Barriers CNS* **8**, 4 (2011).
3. T. Barichello, G. D. Fagundes, J. S. Generoso, S. G. Elias, L. R. Simoes, A. L. Teixeira, Pathophysiology of neonatal acute bacterial meningitis. *J. Med. Microbiol.* **62**, 1781–1789 (2013).
4. S. J. Dando, A. Mackay-Sim, R. Norton, B. J. Currie, J. A. St John, J. A. Ekberg, M. Batzloff, G. C. Ulett, I. R. Beacham, Pathogens penetrating the central nervous system: Infection pathways and the cellular and molecular mechanisms of invasion. *Clin. Microbiol. Rev.* **27**, 691–726 (2014).
5. M. Coureuil, H. Lecuyer, S. Bourdoulous, X. Nassif, A journey into the brain: Insight into how bacterial pathogens cross blood-brain barriers. *Nat. Rev. Microbiol.* **15**, 149–159 (2017).
6. C. H. Wong, J. R. Duque, J. S. C. Wong, C. V. Chan, C. S. I. Lam, Y. M. Fu, K. N. Cheong, G. T. Chua, P. P. Lee, P. Ip, M. H. K. Ho, I. C. K. Wong, G. C. F. Chan, W. H. Leung, S. L. Lee, K. P. Lee, C. C. Shek, M. S. R. Wong, M. S. C. Wong, Y. L. Lau, M. Y. Kwan, Epidemiology and trends of infective meningitis in neonates and infants less than 3 months old in Hong Kong. *Int. J. Infect. Dis.* **111**, 288–294 (2021).
7. J. P. Stevens, M. Eames, A. Kent, S. Halket, D. Holt, D. Harvey, Long term outcome of neonatal meningitis. *Arch. Dis. Child. Fetal Neonatal Ed.* **88**, F179–F184 (2003).
8. L. L. Kenney, E. P. Carter, A. Gil, L. K. Selin, T cells in the brain enhance neonatal mortality during peripheral LCMV infection. *PLOS Pathog.* **17**, e1009066 (2021).
9. L. Travier, M. Alonso, A. Andronico, L. Hafner, O. Disson, P. M. Lledo, S. Cauchemez, M. Lecuit, Neonatal susceptibility to meningitis results from the immaturity of epithelial barriers and gut microbiota. *Cell Rep.* **35**, 109319 (2021).
10. B. Engelhardt, P. Vajkoczy, R. O. Weller, The movers and shapers in immune privilege of the CNS. *Nat. Immunol.* **18**, 123–131 (2017).
11. J. Rustenhoven, J. Kipnis, Brain borders at the central stage of neuroimmunology. *Nature* **612**, 417–429 (2022).
12. T. Croese, G. Castellani, M. Schwartz, Immune cell compartmentalization for brain surveillance and protection. *Nat. Immunol.* **22**, 1083–1092 (2021).
13. T. Masuda, L. Amann, G. Monaco, R. Sankowski, O. Staszewski, M. Krueger, F. Del Gaudio, L. He, N. Paterson, E. Nent, F. Fernandez-Klett, A. Yamasaki, M. Frosch, M. Fliegauf, L. F. P. Bosch, H. Ulupinar, N. Hagemeyer, D. Schreiner, C. Dorrier, M. Tsuda, C. Grothe, A. Joutel, R. Daneman, C. Betsholtz, U. Lendahl, K. P. Knobeloch, T. Lammermann, J. Priller, K. Kierdorf, M. Prinz, Specification of CNS macrophage subsets occurs postnatally in defined niches. *Nature* **604**, 740–748 (2022).
14. B. Engelhardt, R. M. Ransohoff, Capture, crawl, cross: The T cell code to breach the blood–brain barriers. *Trends Immunol.* **33**, 579–589 (2012).
15. J. Derk, H. E. Jones, C. Como, B. Pawlikowski, J. A. Siegenthaler, Living on the edge of the CNS: Meninges cell diversity in health and disease. *Front. Cell. Neurosci.* **15**, 703944 (2021).
16. K. Alves de Lima, J. Rustenhoven, S. Da Mesquita, M. Wall, A. F. Salvador, I. Smirnov, G. Martelossi Cebinelli, T. Mamuladze, W. Baker, Z. Papadopoulos, M. B. Lopes, W. S. Cao, X. S. Xie, J. Herz, J. Kipnis, Meningeal γδ T cells regulate anxiety-like behavior via IL-17a signaling in neurons. *Nat. Immunol.* **21**, 1421–1429 (2020).
17. S. Brioschi, W. L. Wang, V. Peng, M. Wang, I. Shchukina, Z. J. Greenberg, J. K. Bando, N. Jaeger, R. S. Czepielewski, A. Swain, D. A. Mogilenko, W. L. Beatty, P. Bayguinov, J. A. J. Fitzpatrick, L. G. Schuettpelz, C. C. Fronick, I. Smirnov, J. Kipnis, V. S. Shapiro, G. F. Wu, S. Gilfillan, M. Cella, M. N. Artyomov, S. H. Kleinstein, M. Colonna, Heterogeneity of meningeal B cells reveals a lymphopoietic niche at the CNS borders. *Science* **373**, eabf9277 (2021).
18. J. Rustenhoven, A. Drieu, T. Mamuladze, K. A. de Lima, T. Dykstra, M. Wall, Z. Papadopoulos, M. Kanamori, A. F. Salvador, W. Baker, M. Lemieux, S. Da Mesquita, A. Cugurra, J. Fitzpatrick, S. Sviben, R. Kossina, P. Bayguinov, R. R. Townsend, Q. Zhang, P. Erdmann-Gilmore, I. Smirnov, M. B. Lopes, J. Herz, J. Kipnis, Functional characterization of the dural sinuses as a neuroimmune interface. *Cell* **184**, 1000–1016.e27 (2021).
19. A. Merlini, M. Haberl, J. Strauss, L. Hildebrand, N. Genc, J. Franz, D. Chilov, K. Alitalo, C. Flugel-Koch, C. Stadelmann, A. Flugel, F. Odoardi, Distinct roles of the meningeal layers in CNS autoimmunity. *Nat. Neurosci.* **25**, 887–899 (2022).
20. J. Rebejac, E. Eme-Scolan, L. Arnaud Paroutaud, S. Kharbouche, M. Teleman, L. Spinelli, E. Gallo, A. Roussel-Queval, A. Zarubica, A. Sansoni, Q. Bardin, P. Hoest, M. C. Michallet, C. Brousse, K. Crozat, M. Manglani, Z. Liu, F. Ginhoux, D. B. McGavern, M. Dalod, B. Malissen, T. Lawrence, R. Rua, Meningeal macrophages protect against viral neuroinfection. *Immunity* **55**, 2103–2117.e10 (2022).
21. Z. Fitzpatrick, G. Frazer, A. Ferro, S. Clare, N. Bouladoux, J. Ferdinand, Z. K. Tuong, M. L. Negro-Demontel, N. Kumar, O. Suchanek, T. Tajsic, K. Harcourt, K. Scott, R. Bashford-Rogers, A. Helmy, D. S. Reich, Y. Belkaid, T. D. Lawley, D. B. McGavern, M. R. Clatworthy, Gut-educated IgA plasma cells defend the meningeal venous sinuses. *Nature* **587**, 472–476 (2020).
22. H. Van Hove, L. Martens, I. Scheyltjens, K. De Vlaminck, A. R. Pombo Antunes, S. De Prijck, N. Vandamme, S. De Schepper, G. Van Isterdael, C. L. Scott, J. Aerts, G. Berx, G. E. Boeckxstaens, R. E. Vandenbroucke, L. Vereecke, D. Moechars, M. Guilliams, J. A. Van Ginderachter, Y. Saeys, K. Movahedi, A single-cell atlas of mouse brain macrophages reveals unique transcriptional identities shaped by ontogeny and tissue environment. *Nat. Neurosci.* **22**, 1021–1035 (2019).
23. K. Kierdorf, T. Masuda, M. J. C. Jordao, M. Prinz, Macrophages at CNS interfaces: Ontogeny and function in health and disease. *Nat. Rev. Neurosci.* **20**, 547–562 (2019).
24. K. De Vlaminck, H. Van Hove, D. Kancheva, I. Scheyltjens, A. R. Pombo Antunes, J. Bastos, M. Vara-Perez, L. Ali, M. Mampay, L. Deneyer, J. F. Miranda, R. Cai, L. Bouwens, D. De Bundel, G. Caljon, B. Stijlemans, A. Massie, J. A. Van Ginderachter, R. E. Vandenbroucke, K. Movahedi, Differential plasticity and fate of brain-resident and recruited macrophages during the onset and resolution of neuroinflammation. *Immunity* **55**, 2085–2102.e9 (2022).
25. S. S. Kang, D. B. McGavern, Lymphocytic choriomeningitis infection of the central nervous system. *Front. Biosci.* **13**, 4529–4543 (2008).
26. D. Moskophidis, F. Lechner, H. Pircher, R. M. Zinkernagel, Virus persistence in acutely infected immunocompetent mice by exhaustion of antiviral cytotoxic effector T cells. *Nature* **362**, 758–761 (1993).
27. J. V. Kim, S. S. Kang, M. L. Dustin, D. B. McGavern, Myelomonocytic cell recruitment causes fatal CNS vascular injury during acute viral meningitis. *Nature* **457**, 191–195 (2009).
28. J. Cui, H. Xu, M. K. Lehtinen, Macrophages on the margin: Choroid plexus immune responses. *Trends Neurosci.* **44**, 864–875 (2021).
29. D. Schafflick, J. Wolbert, M. Heming, C. Thomas, M. Hartlehnert, A. L. Borsch, A. Ricci, S. Martin-Salamanca, X. Li, I. N. Lu, M. Pawlak, J. Minnerup, J. K. Strecker, T. Seidenbecher, S. G. Meuth, A. Hidalgo, A. Liesz, H. Wiendl, G. Meyer Zu Horste, Single-cell profiling of CNS border compartment leukocytes reveals that B cells and their progenitors reside in non-diseased meninges. *Nat. Neurosci.* **24**, 1225–1234 (2021).

30. D. Mrdjen, A. Pavlovic, F. J. Hartmann, B. Schreiner, S. G. Utz, B. P. Leung, I. Lelios, F. L. Heppner, J. Kipnis, D. Merkler, M. Greter, B. Becher, High-dimensional single-cell mapping of central nervous system immune cells reveals distinct myeloid subsets in health, aging, and disease. *Immunity* **48**, 380–395.e6 (2018).
31. M. Vanlandewijck, L. He, M. A. Mae, J. Andrae, K. Ando, F. Del Gaudio, K. Nahar, T. Lebouvier, B. Lavina, L. Gouveia, Y. Sun, E. Raschperger, M. Rasanen, Y. Zarb, N. Mochizuki, A. Keller, U. Lendahl, C. Betsholtz, A molecular atlas of cell types and zonation in the brain vasculature. *Nature* **554**, 475–480 (2018).
32. J. Kalucka, L. de Rooij, J. Goveia, K. Rohlenova, S. J. Dumas, E. Meta, N. V. Conchinha, F. Taverna, L. A. Teuwen, K. Veys, M. Garcia-Caballero, S. Khan, V. Geldhof, L. Sokol, R. Chen, L. Treps, M. Borri, P. de Zeeuw, C. Dubois, T. K. Karakach, K. D. Falkenberg, M. Parys, X. Yin, S. Vinckier, Y. Du, R. A. Fenton, L. Schoonjans, M. Dewerchin, G. Eelen, B. Thienpont, L. Lin, L. Bolund, X. Li, Y. Luo, P. Carmeliet, Single-cell transcriptome atlas of murine endothelial cells. *Cell* **180**, 764–779.e20 (2020).
33. M. M. Polfliet, P. J. Zwijnenburg, A. M. van Furth, T. van der Poll, E. A. Dopp, C. Renardel de Lavalette, E. M. van Kesteren-Hendrikx, N. van Rooijen, C. D. Dijkstra, T. K. van den Berg, Meningeal and perivascular macrophages of the central nervous system play a protective role during bacterial meningitis. *J. Immunol.* **167**, 4644–4650 (2001).
34. C. R. Melo-Silva, M. I. Roman, C. J. Knudson, L. Tang, R. H. Xu, M. Tassetto, P. Dolan, R. Andino, L. J. Sigal, Interferon partly dictates a divergent transcriptional response in poxvirus-infected and bystander inflammatory monocytes. *Cell Rep.* **41**, 111676 (2022).
35. J. Guarner, P. W. Greer, A. Whitney, W. J. Shieh, M. Fischer, E. H. White, G. M. Carlone, D. S. Stephens, T. Popovic, S. R. Zaki, Pathogenesis and diagnosis of human meningococcal disease using immunohistochemical and PCR assays. *Am. J. Clin. Pathol.* **122**, 754–764 (2004).
36. A. A. Lackner, M. O. Smith, R. J. Munn, D. J. Martfeld, M. B. Gardner, P. A. Marx, S. Dandekar, Localization of simian immunodeficiency virus in the central nervous system of rhesus monkeys. *Am. J. Pathol.* **139**, 609–621 (1991).
37. J. M. Puccini, C. M. Ruller, S. M. Robinson, K. A. Knopp, M. J. Buchmeier, K. S. Doran, R. Feuer, Distinct neural stem cell tropism, early immune activation, and choroid plexus pathology following coxsackievirus infection in the neonatal central nervous system. *Lab. Invest.* **94**, 161–181 (2014).
38. D. R. Chadwick, Viral meningitis. *Br. Med. Bull.* **75-76**, 1–14 (2005).
39. J. V. Forrester, P. G. McMenamin, S. J. Dando, CNS infection and immune privilege. *Nat. Rev. Neurosci.* **19**, 655–671 (2018).
40. P. Solar, A. Zamani, L. Kubickova, P. Dubovy, M. Joukal, Choroid plexus and the blood-cerebrospinal fluid barrier in disease. *Fluids Barriers CNS* **17**, 35 (2020).
41. C. Schwerk, T. Tenenbaum, K. S. Kim, H. Schroten, The choroid plexus-a multi-role player during infectious diseases of the CNS. *Front. Cell. Neurosci.* **9**, 80 (2015).
42. R. E. Watson, J. M. Desesso, M. E. Hurtt, G. D. Cappon, Postnatal growth and morphological development of the brain: A species comparison. *Birth Defects Res. B Dev. Reprod. Toxicol.* **77**, 471–484 (2006).
43. N. R. Saunders, J. J. Dreifuss, K. M. Dziegielewska, P. A. Johansson, M. D. Habgood, K. Mollgard, H. C. Bauer, The rights and wrongs of blood–brain barrier permeability studies: A walk through 100 years of history. *Front. Neurosci.* **8**, 404 (2014).
44. N. R. Saunders, S. A. Liddelow, K. M. Dziegielewska, Barrier mechanisms in the developing brain. *Front. Pharmacol.* **3**, 46 (2012).
45. R. S. Longman, G. E. Diehl, D. A. Victorio, J. R. Huh, C. Galan, E. R. Miraldi, A. Swaminath, R. Bonneau, E. J. Scherl, D. R. Littman, $CX_3CR1^+$ mononuclear phagocytes support colitis-associated innate lymphoid cell production of IL-22. *J. Exp. Med.* **211**, 1571–1583 (2014).
46. B. V. Ineichen, L. Schnell, M. Gullo, J. Kaiser, M. P. Schneider, A. C. Mosberger, N. Good, M. Linnebank, M. E. Schwab, Direct, long-term intrathecal application of therapeutics to the rodent CNS. *Nat. Protoc.* **12**, 104–121 (2017).
47. F. J. Dutko, M. B. Oldstone, Genomic and biological variation among commonly used lymphocytic choriomeningitis virus strains. *J. Gen. Virol.* **64** (Pt 8), 1689–1698 (1983).
48. Y. H. Ban, S. J. Ha, Semi-functional quantitative flow cytometry assay for lymphocytic choriomeningitis virus titration. *Immune Netw* **17**, 307–316 (2017).
49. J. H. Ahn, H. Cho, J. H. Kim, S. H. Kim, J. S. Ham, I. Park, S. H. Suh, S. P. Hong, J. H. Song, Y. K. Hong, Y. Jeong, S. H. Park, G. Y. Koh, Meningeal lymphatic vessels at the skull base drain cerebrospinal fluid. *Nature* **572**, 62–66 (2019).
50. N. Dani, R. H. Herbst, C. McCabe, G. S. Green, K. Kaiser, J. P. Head, J. Cui, F. B. Shipley, A. Jang, D. Dionne, L. Nguyen, C. Rodman, S. J. Riesenfeld, J. Prochazka, M. Prochazkova, R. Sedlacek, F. Zhang, V. Bryja, O. Rozenblatt-Rosen, N. Habib, A. Regev, M. K. Lehtinen, A cellular and spatial map of the choroid plexus across brain ventricles and ages. *Cell* **184**, 3056–3074.e21 (2021).
51. M. M. McCausland, S. Crotty, Quantitative PCR technique for detecting lymphocytic choriomeningitis virus in vivo. *J. Virol. Methods* **147**, 167–176 (2008).
52. M. Hagemann-Jensen, C. Ziegenhain, P. Chen, D. Ramskold, G. J. Hendriks, A. J. M. Larsson, O. R. Faridani, R. Sandberg, Single-cell RNA counting at allele and isoform resolution using Smart-seq3. *Nat. Biotechnol.* **38**, 708–714 (2020).
53. S. C. van den Brink, F. Sage, A. Vertesy, B. Spanjaard, J. Peterson-Maduro, C. S. Baron, C. Robin, A. van Oudenaarden, Single-cell sequencing reveals dissociation-induced gene expression in tissue subpopulations. *Nat. Methods* **14**, 935–936 (2017).

**Acknowledgments:** We thank S.-J. Ha (Yonsei University, Korea) for sharing LCMV-Arm strain, K. Soon Kim and C. D. Surh (IBS/POSTECH, Korea) for sharing CX3CR1-DTR mice, and S. Seo and J. Jung for technical assistance. **Funding:** This study was supported by the Institute for Basic Science (IBS-R025-D1-2015, to G.Y.K.) funded by the Ministry of Science, ICT and Future Planning, Korea. **Author contributions:** Y.-C.K. and J.H.A. conceptualized the project. Y.-C.K., J.H.A., H.J., and M.J.Y. developed the methods. Y.-C.K., J.H.A., H.J., M.J.Y., S.P.H., and J.-H.Y. performed the experiments. Y.-C.K., J.H.A., H.J., and J.-H.Y. analyzed the data. S.-H.K., T.N.G., and Y.-M.K. provided resources. J.H.A. contributed to visualization and curation of data. Y.-C.K. wrote the manuscript. J.H.A., H.J.L., Y.-M.K., and G.Y.K. reviewed and edited the manuscript and provided supervision. G.Y.K. administered the project and provided funding. **Competing interests:** The authors declare that they have no competing interests. **Data and materials availability:** scRNA-deq data are available in National Center for Biotechnology Information's Gene Expression Omnibus under accession numbers GSE209575 and GSE229300. All data needed to evaluate the conclusions in the paper are present in the paper or the Supplementary Materials.

Submitted 10 January 2023
Accepted 24 July 2023
Published 6 October 2023
10.1126/sciimmunol.adg6155

Science Immunology

# Immaturity of immune cells around the dural venous sinuses contributes to viral meningoencephalitis in neonates

Young-Chan Kim, Ji Hoon Ahn, Hokyung Jin, Myung Jin Yang, Seon Pyo Hong, Jin-Hui Yoon, Sang-Hoon Kim, Tirhas Niguse Gebre, Hyuek Jong Lee, You-Me Kim, and Gou Young Koh

*Sci. Immunol.* **8** (88), eadg6155. DOI: 10.1126/sciimmunol.adg6155



*Science Immunology* (ISSN 2470-9468) is published by the American Association for the Advancement of Science. 1200 New York Avenue NW, Washington, DC 20005. The title *Science Immunology* is a registered trademark of AAAS.